Diurnal differences in tropical maritime anvil cloud evolution

Blaž Gasparini*

University of Washington, Seattle, Washington, USA, now at University of Vienna, Vienna, Austria

Adam B. Sokol

University of Washington, Seattle, Washington, USA

Casey J. Wall

Scripps Institution of Oceanography, San Diego, California, USA

Dennis L. Hartmann, Peter N. Blossey

University of Washington, Seattle, Washington, USA

**Corresponding author*: Blaž Gasparini, blaz.gasparini@univie.ac.at

ABSTRACT

Satellite observations of tropical maritime convection indicate an afternoon maximum in anvil cloud fraction that cannot be explained by the diurnal cycle of deep convection peaking at night. We use idealized cloud-resolving model simulations of single anvil cloud evolution pathways, initialized at different times of the day, to show that tropical anvil clouds formed during the day are more widespread and longer lasting than those formed at night. This diurnal difference is caused by shortwave radiative heating, which lofts and spreads anvil clouds via a mesoscale circulation that is largely absent at night, when a different, longwave-driven circulation dominates. The nighttime circulation entrains dry environmental air that erodes cloud top and shortens anvil lifetime. Increased ice nucleation in more turbulent nighttime conditions supported by the longwave cloud top cooling and cloud base heating dipole cannot overcompensate for the effect of diurnal shortwave radiative heating. Radiative-convective equilibrium simulations with a realistic diurnal cycle of insolation confirm the crucial role of shortwave heating in lofting and sustaining anvil clouds. The shortwave-driven mesoscale ascent leads to daytime anvils with larger ice crystal size, number concentration, and water content at cloud top than their nighttime counterparts.

Significance statement. Deep convective activity and rainfall peak at night over the tropical oceans. However, anvil clouds that originate from the tops of deep convective clouds reach their largest extent in the afternoon hours. We study the underlying physical mechanisms that lead to this discrepancy by simulating the evolution of anvil clouds with a high-resolution model. We find that the absorption of sunlight by ice crystals lofts and spreads the daytime anvil clouds over a larger area, increasing their lifetime, changing their properties and thus influencing their impact on climate. Our findings show that it is not only important to simulate the correct onset of deep convection but also to correctly represent anvil cloud evolution for skillful simulations of the tropical energy balance.

1. Introduction

Anvil clouds are both the most frequent and the most radiatively important cloud type in tropical deep convective regions (Hartmann and Berry 2017; Berry and Mace 2014). On average they exert strong shortwave (SW) and longwave (LW) cloud radiative effects (CRE) and therefore significantly modulate both the incoming and outgoing radiative fluxes in the tropical atmosphere. However, their instantaneous effects on both the top-of-the-atmosphere (TOA) radiative fluxes as well as the radiative heating within the atmosphere are strongly influenced by the diurnal cycle of insolation. During the day, an optically thick, fresh anvil cloud will have a strong net negative TOA CRE of up to -500 W m^{-2}, dominated by the strong SW shading effect due to its large albedo. On the other hand, at night the net CRE will be composed only of the LW component and can exceed 150 W m^{-2}. Given the large diurnal cycle in tropical anvil clouds CRE, it is important for climate models to capture both (1) the correct timing of deep convection and (2) the subsequent evolution and thinning of anvil clouds in order to balance radiative fluxes and correctly simulate of changes in climate.

Over the tropical oceans, the majority of rainfall and upper tropospheric anvil clouds originates in large clusters of deep convective activity called mesoscale convection systems (MCS, see e.g. Houze (2004) for a review). Observational data from tropical maritime regions robustly show a diurnal cycle of MCS activity with a peak in the early morning hours (Gray and Jacobson 1977; Chen and Houze 1997; Randall et al. 1989; Nesbitt and Zipser 2003). Similar diurnal pulses of convection and the associated precipitation have been also observed in the Intertropical convergence zone (Bain et al. 2010; Ciesielski et al. 2018) and in tropical cyclones (Dunion et al. 2014; Bowman and Fowler 2015). The precise mechanisms behind this diurnal cycle are still under debate. Possibilities include the stabilization of the environment during daytime by SW heating (lapse-rate mechanism, Kraus 1963; Randall et al. 1989), a daytime decrease in relative humidity due to SW heating of clear sky areas (Tao et al. 1996; Dai 2001), changes in the large-scale overturning circulation between convective and nonconvective regions (cloudy-clear sky differential radiation mechanism, Gray and Jacobson 1977), insolation-driven changes in sea surface temperatures that can excite convectively coupled equatorial waves (Chen and Houze 1997), and convectively forced diurnal gravity waves originating from nearby land (Mapes et al. 2003; Ruppert et al. 2020). Recent idealized simulations of organized deep convection (Ruppert and Hohenegger 2018) point at the primary importance of the lapse-rate mechanism to strengthen convection at night by the radiative destabilization of the atmosphere by LW cooling. This in turn increases convective heating particularly in the lower troposphere and leads to an increased low level circulation due to a sharp heating gradient between the clear sky region, cooled by LW radiation, and the moist region, warmed by convective heating initiating the cloudy-clear sky differential radiation mechanism. In contrast, during the afternoon hours the SW heating near cloud tops was found to intensify the mesoscale circulation in the upper troposphere.

While numerous studies have so far been dedicated to understanding deep convection, we focus on the evolution of detrained anvil clouds to better understand the processes controlling their decay and explain the discrepancy between the early morning peak in deep convection and the number of MCS and the afternoon peak in anvil cloud cover (Fu et al. 1990; Feofilov and Stubenrauch 2019; Chepfer et al. 2019; Sokol and Hartmann 2020). As a difference from the nighttime MCS that define the diurnal cycle of precipitation (Nesbitt and Zipser 2003), the relatively less frequent daytime MCS lead to substantial climatic effects by producing more extensive anvil cloud shields (Wall et al. 2020).

Recent modeling work shows differences between the diurnal cycles of convective activity and ice water path (IWP, the vertically integrated amount of ice in the atmosphere) over tropical oceans (Ruppert and Klocke 2019). While rainfall peaks in the early morning hours, IWP was shown to have two diurnal maxima: one in the early morning hours, coincident with the peak in rainfall and deep convective activity, and one in the afternoon hours, coincident with the diurnal peak in anvil cloud cover. Ruppert and Klocke (2019) explained the secondary peak in IWP as an anvil cloud response to increased SW heating within clouds that enhances the local mesoscale updraft motion, promoting the formation and maintenance of high ice clouds, which we term the anvil lifting hypothesis. Durran et al. (2009) and Dinh et al. (2010) described a similar circulation response for thin tropical tropopause layer cirrus. A greater knowledge of anvil cloud evolution is needed to bridge the gap in our understanding between the early morning peak in deep convection and the afternoon peak in anvil coverage.

Hartmann and Berry (2017) proposed that radiative heating first promotes the rapid decay of thick anvil clouds until they are thin enough for a LW heating dipole (cloud top cooling combined with the cloud base heating) to support its maintenance. This was subsequently modelled in idealized simulations by Hartmann et al. (2018) who found that radiatively driven turbulence extended the cloud lifetime by supporting within-anvil convection that triggered new ice crystal nucleation. The small, newly nucleated ice crystals are only weakly affected by sedimentation compared with larger, aged ice crystals, therefore prolonging the anvil cloud lifetime. We refer to this mechanism as the microphysical cycling hypothesis. Sokol and Hartmann (2020) used CloudSat-CALIPSO satellite data to show that the radiative structure of heating within anvil clouds drives the distribution of anvil optical thicknesses to peak preferentially at cloud optical depths (COD) between 1 and 2. Anvils of such COD were found to be particularly susceptible to radiative destabilization by both LW and SW radiation and to contain larger ice crystal number concentrations than anvils at slightly higher or lower COD, indicating a possible role of new ice crystal nucleation in anvil cloud maintenance.

An observational study by Wall et al. (2020) used geostationary satellite data to evaluate the anvil lifting and microphysical cycling hypotheses. They evaluated the two hypotheses by comparing observations of daytime and nightime anvil clouds and their persistence. Nighttime anvils are influenced only by LW radiation, and therefore should evolve according to the LW heating-cooling dipole that is central to the microphysical cycling hypothesis. During the day, SW heating dominates, suggesting that anvil lifting is favored. Wall et al. (2020) found strong evidence for the dominant role of SW-initiated daytime anvil lifting that increases anvil cloud lifetime and no indication for excessive new ice crystal formation near anvil cloud top in more persistent daytime anvils.

Deng and Mace (2008) studied the diurnal cycle in anvil cloud properties and air motion with the help of the cloud radar observations from two Tropical Western Pacific (Nauru and Manus) and one midlatitude (Southern Great Plains) Atmospheric Radiation Measurement Program sites. The tropical measurements showed a pronounced diurnal cycle in cloud properties and residual air motion. Cloud top height and cloud geometrical thickness both peak in the early afternoon hours, shortly after the midday peak in in-cloud air motion, and reach a minimum in the early morning hours. Similar variations were also measured in cloud microphysical and optical properties, all peaking in the early afternoon hours. Their results are consistent with Wall et al. (2020) and point at the important role of radiative heating in the maintenance and microphysical structure of anvil clouds.

This study extends recent work to study anvil cloud maintenance from an idealized modeling perspective. We first examine the lifecycles of anvil clouds from a sink perspective, by monitoring the decay of identical thick anvil clouds initialized in the middle of a model domain at different times of day. Similarly to Wall et al. (2020), we take advantage of the diurnal cycle of insolation, further simplified by examining cloud evolution during perpetual night and midday conditions. We support these idealized experiments with an analysis of a statistically representative ensemble of anvil clouds from a simulation in radiative-convective equilibrium (RCE) with a realistic diurnal cycle of insolation. RCE is a simplified description of the climate system, in which radiative cooling of the atmosphere must be balanced by latent heating from convective cloud processes. It is a useful representation of the tropical atmosphere particularly at large spatial and long temporal scales (Jakob et al. 2019). While Ruppert and Hohenegger (2018) and Ruppert and Klocke (2019) investigated diurnal cycle impacts on organized convection, this study focuses on anvil cloud dynamics, circulations, microphysics, and their radiative impacts in non-organized convection.

2. Methods

a. Model

We use the version 6.10 of the System for Atmospheric Modeling (SAM) cloud resolving model (Khairoutdinov and Randall 2003). The model is coupled with the RRTMG radiative transfer model (Mlawer et al. 1997; Iacono et al. 2008) and uses a Smagorinsky-type 1.5-order closure scheme to represent the subgrid-scale motions. The radiation called every sixth, 30-s long, model timestep. The model allows for substepping to ensure the Courant-Friedrich-Levy criterion and is set to use periodic lateral boundary conditions. Microphysical processes are represented with the Predicted Particle Properties (P3) bulk microphysical scheme (Morrison and Milbrandt 2015), version 3.1.4, with the following deviations from the default P3 microphysics:

- The maximum ice crystal number concentration limit is increased from 0.5×10^6 to 10×10^6 kg^{-1} in order to allow for realistic simulations of fresh deep convective outflow with high ice crystal number concentrations (Heymsfield et al. 2017; Jensen et al. 2018; Krämer et al. 2020).

- Freezing in mixed-phase clouds is parameterized following Meyers et al. (1992) with an additional constraint that allows ice nucleation only in the presence of cloud droplets, since deposition freezing is thought to be negligible in mixed-phase conditions (e.g., Ansmann et al. 2008; DeMott et al. 2010; Hoose and Möhler 2012; Lohmann et al. 2016).

- Freezing below the homogeneous freezing temperature of water (-38°C) follows the description of Shi et al. (2015), as implemented in CAM5, CAM6, and E3SM general circulation models. The formulation is largely based on the parameterization by Liu and Penner (2005) that simulates the competition between homogeneous and heterogeneous freezing in cirrus clouds. The competition for vapor between freezing and pre-existing ice crystals follows the description published in Kärcher et al. (2006). The number of ice nuclei considered by the Liu and Penner (2005) parameterization is due to the absence of an interactive aerosol module set to 2 L^{-1}, typical for low aerosol concentration in the upper troposphere of the Tropical Western Pacific (e.g., Gasparini and Lohmann 2016). The number of sulfate aerosols available for homogeneous freezing is set to 20 cm^{-3}.

- The saturation vapor pressure for liquid water and ice is parameterized by the Murphy and Koop (2005) formulation.

The simulated ice cloud properties were found to generally agree with the observed tropical maritime cloud data, despite a small underestimation in cloud water content at temperatures between 0°C and -80°C and the underestimation of ice crystal number at temperatures colder than -60°C. A short model evaluation comparing model output with cloud properties observed in three tropical aircraft field campaigns, consolidated in a uniform dataset by Krämer et al. (2020), can be found in Appendix A.

b. Simulations

We use two different simulation strategies of differing model complexities. In the simplest setup, we initiate a thick ice cloud with uniform ice mixing ratio of about 0.6 g kg^{-1} and a diameter of 60 km in the middle of a 256×256 km model domain, as described in Gasparini et al. (2019). All of the described simulations use 128 vertical levels with the upper tropospheric vertical resolution of 250 m and the horizontal resolution of 1 x 1 km that is able to resolve part of the within-anvil convection that drives a significant proportion of the within-anvil microphysical process rates (Gasparini et al. 2019). The model typically uses two substeps within one model timestep in the first few hours of the simulation, decreasing the effective model timestep from 30 to 15 s. The simulations are initialized without the presence of any mean winds from a typical tropical temperature and moisture profile. The model mean horizontal wind fields are nudged to zero.

The cloud is representative of observed freshly detrained thick anvils in the tropics, with a cloud top altitude at 13 km and cloud base at 8 km. The cloud's initial diameter is set to 60 km in all but small-real and large-real simulations. We simulate the evolution of the cloud by either assuming a realistic diurnal cycle of insolation and varying the simulation starting time or by fixing the insolation to a constant value representing the typical midday (1300 W m^{-2}) or night (0 W m^{-2}) conditions. In addition, we conduct several sensitivity tests with changes to physical processes that influence the ice cloud evolution, namely SW and LW atmospheric cloud radiative effects (ACRE), ice crystal sublimation, ice sedimentation, and ice nucleation (Table 2).

Secondly, we perform a 50-day simulation of a cloud field in RCE with a realistic diurnal cycle of insolation typical for the equator. The simulation is initialized from a temperature and moisture profile generated from the average over the last 20 days of an earlier 100 day-long RCE simulation with a smaller model domain. Only the last 30 days of the hourly model output, after the simulated climate reaches a statistical equilibrium, are considered in this analysis. The sensible and latent heat fluxes are computed interactively. The model typically uses 5-9 substeps within one model timestep, decreasing the effective model timestep from 30 to 3-6 s. The RCE simulations are performed in a 128×128 km domain, which is too small to allow the development of convective organization.

c. Himawari satellite data

We use 3 months (June 1 - August 31 2016) of Himawari-8 geostationary satellite observations (Bessho et al. 2016) of brightness temperature (BT) at the infrared channel (11.2 μm). The downloaded product was subsequently regridded to 0.25° by averaging the native grid pixels within the new grid boundaries. The dataset's temporal resolution is 1 hour.

3. Results

a. Diurnal cycle of brightness temperature from geostationary satellite observations

Figure 1a shows the geostationary satellite measurements of BT in the ocean-covered areas of the Tropical Western Pacific (20°S to 20°N, 130°E to 180°E). The BT roughly corresponds to the cloud top temperature for optically thick clouds with emissivity values near 1 (Protopapadaki et al. 2017). The BT signal from thinner clouds includes a mixture of the clouds' emission and the emission from lower, warmer atmospheric levels. Most of such clouds can be classified as anvil clouds in different stages of their lifecycle. Appendix B contains a detailed discussion explaining why most pixels with BT<290 K correspond to high clouds.

The BT observations are clustered into 10 K bins to better represent the transition from deep convective cores (BT < 210 K) to anvil clouds of various optical thickness (210 < BT < 290 K). The relationship between BT and high cloud COD is explained in more detail in Appendix B. The BT values typical of deep convection occur most often in the early morning hours, while the BT bins associated with anvil clouds peak 7-18 hours later (Fig. 1). Interestingly, the frequency of pixels with BT of 210 - 220 K peaks at 14 local time (LT). This BT bin corresponds to a mixture of weaker deep convective systems that are frequent in the afternoon hours (Nesbitt and Zipser

2003) and thick anvil clouds. This peak is followed by successive peaks in BT bins between 220 and 290 K in the afternoon and evening hours, when deep convective activity remains low (Fig. 1b). The transition from BT maxima of 210-220 K at 14 LT to 250-260 K at 20 LT reflects a BT warming rate of 15 K hour^{-1}. This corresponds to a thinning of the median anvil COD from about 30 to about 2 within 6 hours, as confirmed by a combination of DARDAR cloud profile and MODIS BT data (Appendix B). The thinning slows down after the anvils reach a COD of ~2 that was found to be preferred based on radiative flux considerations (Hartmann and Berry 2017; Sokol and Hartmann 2020). These results agree with a study using the spaceborne lidar data from the CATS instrument that showed an increase in high opaque clouds in the afternoon hours (Chepfer et al. 2019) and another that relied on infrared sounder data (Feofilov and Stubenrauch 2019). Moreover, Sokol and Hartmann (2020) found a larger coverage of anvil clouds in the Tropical Western Pacific and Tropical Indian Ocean during the afternoon A-Train overpass (13.30 LT) compared with the night one (1.30 LT), which is consistent with the observed afternoon peak in the BT bins of 210-260 K.

The clouds from the afternoon/evening anvil cloud peak cannot be generated by the diurnal peak in convective activity that occurs 6-8 hours earlier. While the transition from convective cores to thin anvils can take up to 10 hours, the optically thick phase of anvil evolution that corresponds to BT of up to 220-240 K and COD of 5-15 (Fig. B1) is unlikely to persist in the atmosphere for more than about 5 hours (e.g., Mace et al. 2006; Wall et al. 2020; Jensen et al. 2018; Gasparini et al. 2019, 2021, appendix B of this manuscript). Additional physical mechanisms must therefore play a role in the formation and maintenance of the afternoon and evening anvil clouds. This result is consistent with the work by Wall et al. (2020), which concluded that the daytime anvil clouds must be more persistent and/or more widespread compared with their nighttime counterparts.

b. Idealized simulations

Figure 2 shows the time evolution of the IWP for two identical high clouds initialized at two different times during the diurnal cycle. The first cloud is initialized at 21 LT and undergoes a rapid thinning and spreading until disappearing about 8 hours after the initialization, at 5 LT, just before sunrise. The cloud initialized at 9 LT persists for more than 15 hours, spreading over a larger portion of the domain (Fig. 2b). The clouds initialized at 9 and 21 LT represent the two extremes among clouds initialized throughout the diurnal cycle: on one side the persistent and widespread daytime anvil cloud, and on the other side the shorter lived nighttime anvil. Additional simulations of anvil cloud lifecycles initialized at each of the 24 hours of the day fall in between the selected two cases in terms of IWP, cloud fraction, and cloud persistence (not shown).

The TOA radiative effects also vary significantly depending on the simulation start time. Fig. 3 represents values of SW, LW, and NET CRE averaged over the whole domain and 16 hour duration of the simulations for each of the simulations initialized at different times of the day. Simulations that start in the morning hours (particularly 7-11 LT) lead to a large LW CRE and an even larger SW CRE, with a negative net CRE of -5 to -10 W m^{-2} $\times$ day, when averaged over the entire anvil lifecycle. In contrast, simulations starting in the late evening or night (between approximately 15 and 3 LT) exert no or a very small SW CRE caused by the lack of insolation and a smaller LW CRE due to their smaller extent and shorter lifetime, leading to a net positive integrated CRE of 1 W m^{-2} $\times$ day over the course of the anvil lifecycle. Only a small change in the starting time of the anvil cloud can therefore cause a substantially different net climatic effect.

The radiative effects of anvil clouds with different initialization times vary not only because of insolation differences, but also because of differences in cloud optical properties. Figure 4 shows the COD evolution of a daytime and nighttime simulation composite. Daytime simulations are influenced by strong insolation of 900 W m^{-2} or more in the first 8 hours. The two composites do not differ substantially in the first two hours of the evolution, when the COD distribution of both composites peaks near 100 (Fig. 4a). For a cloud age of 3-5 hours, however, the daytime composite shows a bimodal distribution with COD peaks near 100 and 3, as opposed to thinner nighttime clouds peaking between COD of 3 to 30 (Fig. 4b). A large majority of nighttime clouds of age 6-8 hours are optically thin (Fig. 4c), with COD smaller than 0.5, and disappear almost completely by hour 9-11 of the simulation (Fig. 4d). In contrast, 6- to 11-hour-old daytime anvils cover a large portion of the domain with a COD distribution peak that slowly shifts from $\sim$1 to $\sim$0.1 before fully disappearing at hour 14-16 of the simulation (Fig. 2b).

At this point we further simplify the modeling setup to isolate the differences between the day and night simulations by simulating cloud evolution in perpetual midday conditions with insolation values of 1300 W m^{-2} (referred to as "day-only") and perpetual night conditions (no insolation, referred to as "night-only") as shown by Fig. 5a,b. The IWP evolution of the night cloud strongly resembles the 21 LT case from Fig. 2a, while the day cloud resembles the 9 LT case from Fig. 2b. The main difference between the evolution of the day-only and night-only cases is best represented by the Fig. 6. The daytime anvil is quickly lofted by about 1.5 km due to a strong SW heating that overcompensates the cloud-top LW cooling effect (Fig. 6b). The heating-induced updraft (Fig. 6d) supports higher relative humidities with respect to ice (RH$_{ice}$), limiting the cloud decay by sublimation (not shown). Nevertheless, sublimation remains the largest microphysical tendency due to cloud spreading and mixing with environmental air that is subsaturated with respect to ice (Fig. 7a-c). Despite the SW-driven updraft, the net sedimentation flux remains substantial throughout the first 16 hours of cloud evolution (Fig. 7d). The sinking motion near cloud base that appears in both day-only and night-only simulations (Fig. 6c,d) is caused by latent cooling due to ice crystal sublimation, which is by far the largest ice crystal number sink (Fig. 7e).

On the other hand, the top of the nighttime anvil remains at an approximately constant altitude in the first 2-4 hours of the simulation despite a strong LW cloud top cooling and the associated downdrafts (Fig. 6a,c). At the same time, the center of the cloud undergoes depositional heating, which helps counteract the sinking motion near the cloud top. The latent heating tendency decreases through time, and the cloud gradually dissipates by sublimation and sedimentation (Fig. 7a-c) before completely disappearing within 8 hours of the initialization (Fig. 6a). Sublimation is stronger at night because the cloud sinks down to higher temperatures and lower RH_{ice} that support faster sublimation. Interestingly, there is substantially more ice crystal nucleation at night than there is during the day (Fig. 7f), indicative of a stronger turbulence at night caused by the LW radiative heating dipole and depositional heating within the cloud. The new ice crystal nucleation is expected to prolong the cloud lifetime; however, the sublimation tendency is substantially stronger, leading to a rapid cloud decay. This is confirmed by a simulation in which freezing was not allowed, which show a similar evolution compared to the reference case (Figs. 5a-d and 8a-d).

The diurnal differences in cloud evolution are also modulated by differences in cloud top circulation. The night-only simulation develops a two cell circulation (Fig. 9a,b), with a main, lower branch driving the spreading of the cloud and a secondary branch near cloud top, similar to what was shown by Gasparini et al. (2019) for daily average conditions. The upper circulation cell, driven by LW cooling, largely disappears due to SW heating in the day-only case. The day-only simulation develops only one circulation cell that leads to strong spreading and lofting of the cloud (Fig. 9c,d), keeping the cloud top at near saturated conditions. The nighttime circulation erodes the cloud from the top by mixing in subsaturated environmental air which decreases the cloud top altitude and accelerates the cloud decay.

1) Sensitivity simulations

A sensitivity test in which the clouds are trasparent to radiation (no-ACRE) shows little difference in cloud evolution between the two insolation setups (Figs. 5e,f in 8e,f). The no-ACRE clouds do not spread and thin, but just slowly sediment out of the atmosphere and sublimate as shown by the decreasing cloud top altitude in Fig. 8e,f. The absence of the radiatively-driven circulation in the no-ACRE nighttime cloud prevents cloud spreading and mixing with the subsaturated environmental air and prolongs the cloud lifetime when compared with the night-only simulation. The domain average radiative impact of such slowly sedimenting and sublimating clouds is quite limited due to their small surface area and dominated by SW CRE, leading to a net cooling effect on climate (not shown).

The no-sublimation sensitivity tests lead to long-lived clouds in both day and night simulations (Fig. 5g,h). The night no-sublimation experiment contains several times larger IWP than the day case (confront Fig. 5g and h). This is caused by the lower cloud temperature in the daytime one, when the cloud top is lofted from about 13 to about 16 km (Fig. 8g,h), experiencing about 20 K colder temperatures. The colder temperatures inhibit a large portion of the depositional growth of ice in the higher and colder day cloud compared with the night cloud.

Given the importance of the sedimentation flux, we analyze an additional sensitivity simulation in which there is no ice crystal sedimentation (no-sedimentation). Fig. 5i,j show very similar IWP time evolution in the two simulations, despite a higher cloud top in the day simulation (Fig. 8i,j). Interestingly, the strong LW heating near cloud base and latent heating by deposition within the cloud gradually overcompensate the LW cooling related downdraft near cloud top in the nighttime simulation. Between hour 5 and 15 of the simulation, when the cloud is thinner due to its spreading in the surrounding clear sky air, the heating-induced updraft velocity lofts it about 2 km (Fig. 8i). The sensitivity tests reveal that cloud radiative heating, sublimation, and sedimentation all shape anvil cloud evolution.

Additional sensitivity tests are performed to investigate how the diurnal cycle effect on cloud evolution depends on cloud size. We hypothesize that a larger initial cloud initialized at 21 LT will experience proportionally less entertainment of drier environmental air, which is maximized in absence of SW heating at night. In order to test this, we performed experiments in which the initial cloud diameter was halved (small-real) and doubled (large-real) compared with the control simulation (ctrl-real) with a diameter of 60 km. The clouds with which the simulations are initialized represent freshly detrained anvils, tightly related to the actively convective part of the MCS. An actively convective surface area larger than 5000 km^2 (the equivalent of an initial cloud diameter of 40 km) is therefore unlikely to exist within a single MCS (Houze 2004).

Figure 10 shows the ratio of the domain averaged IWP and cloud fraction between the nighttime cloud initialized at 21 LT and the daytime cloud initialized at 9 LT. The smaller the fraction, the quicker the nighttime cloud decays in comparison to its daytime equivalent, and the larger is the impact of the diurnal cycle on the cloud evolution. As expected, both IWP and cloud fraction are smaller in the nighttime clouds; the fraction is thus below 1 for all cases for most of the cloud lifetimes. The impact of the diurnal cycle is thus the largest for the small-real cloud and smallest for the large-real cloud. The diurnal cycle effect on cloud evolution therefore decreases with the increase of the initial cloud size.

c. RCE simulations

To understand whether the day-night differences seen in simulations of individual clouds above are present in extended simulations of clouds and convection, we perform additional simulations of a cloud field in RCE. In Fig. 11, selected variables are plotted as a function of IWP, with IWP decreasing from left to right. This gives an intuitive view of the anvil cloud evolution, from freshly detrained anvils at the highest IWP, to aged thin anvil clouds at low IWP (please refer to the Appendix C for a detailed description of the IWP binned perspective on anvil cloud evolution). This view is confirmed by Fig. 11a,b that show how much time has elapsed since a parcel was last in a buoyant cloudy updraft with vertical velocity larger than 1 m s^{-1}, which is representative of deep convective cores. This is therefore a meaningful proxy for anvil cloud age, which increases from about 1.5 hours near the main deep convective detrainment level at around 12 km altitude to about 10 hours at low IWP values, typical for aged anvil clouds or in-situ formed cirrus.

The variables are shown separately as an average between 0-4 LT (typical for nighttime conditions, left column), 12-16 LT (typical for daytime conditions, middle column) and the anomaly between the two times (right column). The general pattern of cloud age does not change significantly between day and night: however, the transition from a high IWP deep convective core to thin anvil is faster at night. The 6 hour isochrone reaches the 50th IWP percentile at night (Fig. 11a) but only the 70th percentile during the day (Fig. 11b), implying faster nighttime cloud decay. Moreover, the clouds at levels above 12 km in all IWP bins except the highest few are fresher during daytime (Fig. 11c). Therefore, while the level of convective detrainment remains nearly the same throughout the day, the subsequent anvil cloud evolution takes a different pathway, which is, as in the idealized simulations, modulated by differences in ACRE. Strong LW cooling dominates the cloud top at high IWP percentiles (thick anvil clouds) during the night, with LW heating below (Fig. 11d). In the day, the SW heating is strong enough to neutralize the LW cooling, leading to no significant ACRE near the tops of thick anvil clouds (Fig. 11e). However, the SW heating effect dominates in the intermediate and thin anvils and induces a slow mesoscale updraft motion of about 1-7 cm s^{-1} (Fig. 11h) that supports the maintenance of anvils. In contrast, the nighttime cloud top cooling leads to a downdraft motion that reaches values of about 5 cm s^{-1} on average (Fig. 11g), enhancing the removal of ice crystals by sedimentation (Fig. 7d).

The streamfunction, computed as in Gasparini et al. (2019), shows a strong main upper tropospheric branch with a maximum near the main level of deep convective outflow at 12 km, extending throughout most of the domain at all times (Fig. 11j). At night, a secondary circulation driven by the LW cloud-top cooling flows in the opposite direction, similarly to what shown in Fig. 9a for the night-only simulation. This upper level circulation pattern nearly disappears during the day (Fig. 11k). In addition, the peak of the main circulation that drives the spreading of anvil clouds shifts towards higher altitudes and lower IWP percentiles (thinner anvil clouds) during the day, driven by the SW ACRE.

ACRE-driven dynamical changes lead also to changes in RH_{ice}. Figure 12 provides a more detailed perspective on diurnal changes in RH_{ice}, temperature, and updraft velocities in thick anvil clouds (88-98 IWP percentile, COD range of 10 to 50), intermediately thick anvils (70-88 IWP percentile, COD range of 2.5 to 10) and thin anvils (30-70 IWP percentile, COD range of 1-2.5). The strong radiatively driven ascent in thick anvils increases RH_{ice} during daytime hours (Fig. 12a). However, the increase is only modest, rarely exceeding 1 % and is not observed in thinner anvil clouds. In contrast, the RH_{ice} decreases during the day in the rest of the model domain, particularly in the clear sky areas (Fig. 12b). This is caused by a combination of weak diurnal heating of the clear sky portion of the domain by the SW absorption by water vapor (Fig. 12c) and conservation of mass, which implies a stronger compensating subsidence in clear sky regions at times of elevated upward mass flux in the anvil-covered part of the domain. The simulated diurnal changes in clear sky RH_{ice} are comparable to those in Megha-Tropique satellite observations (Chepfer et al. 2019). The dynamical cooling effect caused by within-anvil updraft motions during daytime is not strong enough to compensate for the heating due to the SW absorption, leading to a slightly increased anvil temperature in the afternoon hours (Fig. 12c).

1) Diurnal variations in turbulence and mesoscale ascent

Figure 12d confirms that the frequency of updraft motions within anvil clouds (defined as updrafts > 1 cm s^{-1}) is higher during daytime hours, with a clear peak around 12 LT for thick anvils, and a similar, but less pronounced peak for intermediate anvils peaking 1-2 hours later in the early afternoon. The peak in updraft frequency within thin anvils is delayed until approximately 16 LT due to a slow dynamical response to their weak heating rate. Interestingly, the occurrence frequency of strong updraft motions, representative of turbulence, shows the opposite behavior, peaking in the night, and reaching minimum values during the afternoon hours (Fig. 12e). Turbulence is favored when there is a heating dipole comprised of cloud-top radiative cooling and internal heating due to radiation and latent heat release, which initiates in-cloud convection (Fig. 11d). The standard deviation of in-cloud updraft velocity (Fig. 12f) shows a similar diurnal cycle, with a nighttime peak and a minimum at about 14 LT for both thick and intermediate anvil clouds, and a delayed afternoon minimum for thin anvils at about 17 LT.

2) Diurnal variations in ice microphysical properties

Anvil cloud ice mixing ratio can vary from values close to 1 g kg^{-1} in fresh anvils to 10^{-3} g kg^{-1} in thin anvil clouds (Fig. 13a,b). Similarly, the simulated ice crystal number concentrations often exceed 1000 L^{-1} in fresh anvils, with concentrations between 5 and 100 L^{-1} typical for thinner anvil clouds (Fig. 13d,e). Ice crystal effective radius is inversely proportional to altitude; the model simulates particle sizes of about 70 μm at 8 km altitude, which decreases to about 10 μm at 15 km as a result of gravitational settling of larger ice crystals and the slowdown of depositional growth at cold temperatures (van Diedenhoven et al. 2020). Ice crystals are larger in deep convective cores and fresh anvils, as the strong updrafts can overcompensate sedimentation of both smaller and larger ice crystals (Fig. 13g,h).

Changes in ACRE lead to differences in anvil cloud microphysical properties. Both ice mixing ratio and ice crystal number concentration are more top heavy in the day compared with night (Fig. 13a-f). Most of the simulated anvil ice crystals originate from freezing within deep convective updrafts. The variations in anvil ice crystals size and number are therefore indicative of changes in detrained air parcel trajectories and not of new nucleation events outside of deep convective cores as demonstrated by the small influence of ice nucleation on the evolution of idealized cloud simulations (Figs. 5c,d and 8c,d). Upward motions during the day counteract sedimentation and therefore support anvil clouds with larger ice crystal radii, particularly for intermediately thick and thin anvil clouds (Fig. 13h).

3) Diurnal variations in convective updrafts and freshly detrained ice microphysical properties

Diurnal variations in anvil cloud properties may partially depend also on the convective processes, particularly the updraft velocity and its microphysical implications. Figure 14a,b shows the mean values of updraft velocity in cloudy updrafts with vertical velocities larger than 1 m s^{-1} that are positively buoyant and its anomalies with respect to diurnal mean values. The convective updraft velocities do not vary much throughout the day, with substantial anomalies occurring only above the peak anvil detrainment level, where deep convective updrafts occur infrequently, leading due to small sample sizes only to random fluctuations in updraft strength. Moreover, the fluctuations largely disappear when computing median instead of mean velocities (not shown). Panels 14c-h similarly show mean values (left column) and their anomalies with respect to diurnal mean (right column) for ice cloud properties of freshly detrained anvil clouds, with a cloud age of less than 1 hour. The varibility of freshly detrained ice properties at the main detrainment level between 9 and 13 km is very limited and possibly related to variations in cumulus congestus and not anvil clouds.

4. Discussion

This work agrees with recent modeling (Ruppert and Hohenegger 2018; Ruppert and Klocke 2019) and observational studies (Deng and Mace 2008; Wall et al. 2020; Sokol and Hartmann 2020) that point at the important role of daytime cloud heating by SW absorption in modulating the anvil lifecycle. Our results confirm both hypotheses posed by Ruppert and Klocke (2019): SW heating of anvils causes a daytime upper tropospheric increase in upward motion and consequently leads to longer lived and more widespread anvil clouds. While Ruppert and Klocke (2019) and Ruppert and O'Neill (2019) considered the role of SW heating in organized convection, our work points out at an important role of the SW-driven ascent for non-organized convective systems, that were a focus of our idealized and RCE simulations. SW radiative heating was based on ground radar measurements hypothesized to drive diurnal variations in both cloud macrophysical and microphysical properties (Deng and Mace 2008), which was largely confirmed by our idealized model simulations.

Our work shows that despite being less frequent, daytime MCS play an important role in the climate system by spawning anvil clouds supported by solar heating that ultimately cover a larger fraction of the tropical maritime areas compared to anvils initalized in more frequent nocturnal and early morning MCS. MCS were previously shown to contribute most to the total precipitation in most of the tropics, thus controlling also the diurnal cycle of precipitation with a peak in the early morning hours (Zipser and LeMone 1980; Fu et al. 1990), when the number of MCS is maximal. This coincides with the diurnal BT frequency peak for BT<210 K shown in Fig. 1. In contrast, the relatively less frequent daytime convection and MCS drives the afternoon-evening peak in anvil cloud fraction of decreasing cloud optical depths and thus exhibits a strong control on both SW and LW radiative fluxes.

Tropical anvil clouds are affected not only by slow, laminar, mesoscale circulations associated with the diurnally enhanced in-cloud ascent but also by in-cloud convection. Ground radar measurements from the Tropical Western Pacific presented in Wall et al. (2020) show a larger variance in updraft velocities during the night for thick and intermediate anvil clouds, which is consistent with our findings and indicative of higher turbulence. The cloud top ice crystal number was found to be smaller during night in CloudSat-CALIPSO observations (Wall et al. 2020), despite more turbulent environmental conditions, favorable for new ice nucleation, which is agreement with our modeling results. Our simulations indicate that most of ice crystals detrain from deep convection, and thus subsequent ice nucleation within or at the edge of anvil clouds is not frequent enough to significantly affect the ice crystal number budget. This is in contrast to Hartmann et al. (2018) who found that new ice nucleation is an important mechanism prolonging anvil cloud lifetime. However, their simulations used a fully cloud covered domain, in which the cloud could not dissipate by spreading into neighboring air. This spreading also disperses the cloud's turbulent kinetic energy over a larger area, decreasing the potential for in-cloud convection (Schmidt and Garrett 2013).

Our work offers support for hysteresis in anvil clouds. Anvil evolution takes a different pathway depending on the amount of insolation during the fresh anvil stage. Anvils subjected to insolation of about 800 W m^{-2} or more maintain a constant cloud top height or even undergo lofting and enhanced spreading that cannot be achieved at night, in the early morning, or in the late afternoon (Fig. 15). This is consistent with the observational finding of Sokol and Hartmann (2020) that fresh anvil clouds sink after detrainment at night but are maintained at higher altitudes during the day. They speculated that the altitude, geometric thickness, and radiative heating rates of aged anvil clouds are influenced by the time of day at which the cloud was detrained. Our findings are consistent with this notion.

We also find that the time at which an anvil cloud is detrained influences the cloud's climatic effects. In RCE simulations, deep convective activity peaks at 5 LT. A mere one-hour shift in the timing of this peak could lead to substantially different anvil net CRE. A hypothetical shift of convective detrainment from 5 to 6 LT would lead to a 3 W $m^{-2} \times day^{-1}$ more negative integrated net CRE (or a 2 W $m^{-2} \times day^{-1}$ more positive integrated net CRE in the case of an opposite shift from 5 to 4 LT) based on the simulated single cloud evolution simulations (Fig. 3). A modeling study using a general circulation model in present and 4K warmer climate found a 4-hour delayed convective activity peak in the warmer climate compared with the reference climate, that contributed to a significant negative diurnal component of the cloud feedback (Gasparini et al.

2021). However, more work is needed to understand whether a change in the diurnal cycle of deep convection and anvil clouds in a warmer climate is a robust response to increased greenhouse effect or only an artifact of a single climate modeling study.

5. Conclusions

In this study we first analyzed the diurnal variations in BT from Himawari geostationary satellite observations in the Tropical Western Pacific, which indicate an afternoon diurnal peak in anvil cloud fraction, in contrast to the early morning peak in deep convective activity and rainfall. The large time gap between the peak in convection and in anvil cloud fraction implies that the evolution of anvil clouds must differ between daytime and nighttime. In particular, the daytime anvils must be more widespread and/or long-lived compared with the nighttime anvils.

In order to explain this observed behavior we used idealized simulations with the SAM cloud-resolving model. We initialized each of the simulations with a cylindrical-shaped cloud, comparable to freshly detrained, thick anvil clouds and let the cloud evolve freely. The only difference between the simulations is their starting time; we started identical clouds at each hour, from 0 to 23 LT. The clouds' evolution pathways differ substantially in terms of cloud lifetime, coverage, and climatic effects. The absorption of SW radiation by ice crystals was found to be the key driver of diurnal differences between simulated anvil clouds (Fig. 15). The anvil clouds exposed to insolation of about 800 W m^{-1} or more are able to support a mesoscale ascent that partially counteracts the sedimentation of ice crystals and supports favorable conditions for cloud maintenance by keeping the cloudy parcels saturated. The heating that the cloud experiences in tropical regions around noon can be strong enough to loft the cloud. Moreover, the SW heating intensifies the radiatively driven circulation, leading to a faster spreading of the cloud that in turn covers a larger surface area (Fig. 15). On the other hand, nighttime anvil cloud top is dominated by the LW cooling, which drives a circulation near cloud top that entrains drier environmental air into the cloud, eroding the cloud top and shortening its lifetime. This effect weakens for more extensive anvil cloud systems.

The RCE simulation with a realistic diurnal cycle provides additional support for the results of the idealized simulations. The SW-driven mesoscale ascent both increases the cloud top altitude during the day and allows more and larger ice crystals near the anvil cloud top. Despite experiencing elevated levels of turbulence that trigger more ice nucleation, nighttime anvils contain fewer ice crystals near cloud top where nucleation is most likely to occur. The source of ice crystal number by in-situ ice nucleation was found to be only of secondary importance for anvil evolution, behind the dominant source of ice crystals by cloud droplet freezing within deep convective updrafts. Cloud properties were not found to vary substantially at or immediately after the deep convective detrainment.

The evolution and climatic effect of anvil clouds largely differ based on the time of cloud initialization. It is crucial that models successfully reproduce the timing of deep convection and correctly represent the radiative-microphysical-dynamical interactions driving anvil decay. Only in this way can climate and cloud-resolving models successfully reproduce the tropical energy balance and lend credibility to their projections of future climate.

Acknowledgments. We acknowledge the constructive comments by Jay Mace and 3 anonymous reviewers that helped improve the manuscripts. The comments by Martina Krämer helped in the interpretation of the model comparison with the observations. BG acknowledges support by the Swiss National Science Foundation project P400P2_191112 and by the National Science Foundation under Grant AGS-1549579. CJW is supported by the NOAA Climate and Global Change Postdoctoral Fellowship Program, administered by UCAR's Cooperative Programs for the Advancement of Earth System Science (CPAESS) under award #NA18NWS4620043B. ABS acknowledges support from NASA grant 80NSSC20K1613. PNB acknowledges support from the NSF under grant OISE-1743753.

Data availability statement. The Himawari-8 data were obtained from the Atmospheric Science Data Center of the NASA Langley Research Center and are available at https://earthdata.nasa.gov/. The satellite data from the A-Train Integrated CALIPSO, CloudSat, CERES were obtained from https://search.earthdata.nasa.gov. The Cirrus Guide II in-situ cloud data set is accessible under https://doi.org/10.34730/266ca2a41f4946ff97d874bfa458254c (Krämer et al. 2020). Data and analysis scripts necessary to generate the figures in the manuscript are available at 10.5281/zenodo.5534641.

APPENDIX A

Comparison of modelled tropical ice cloud properties with in-situ data

Cloud properties from a 30-day long free running RCE simulation are compared with 69 hours of aircraft observational data used in Krämer et al. (2020) from 3 field campaigns in the Tropical Western Pacific ocean, namely: The NASA Airborne Tropical TRopopause EXperiment (ATTREX) (Jensen et al. 2017), The NASA Pacific Oxidants, Sulfur, Ice, Dehydration, and cONvection (POSIDON) Experiment (https://espo.nasa.gov/posidon), and The Convective Transport of Active Species in the Tropics (CONTRAST) Experiment (Pan et al. 2017). ATTREX and POSIDON measurements were focused on the tropical tropopause region, collecting data mainly from thin cirrus at temperatures between -90°C and -60°C. In CONTRAST Experiment, as a difference, clouds were sampled between the marine boundary layer and the bottom of the tropical tropopause region at about 14 km altitude, including the altitude of main deep convective detrainment. The plotted quantities refer to ice only properties at temperatures colder than -35°C and a mixture of cloud ice and liquid in the mixed-phase temperature range.

Despite its simple simulation setup, the model is able to reproduce many features of the tropical climate, in particular the balance between the radiative cooling of the cloud-free atmosphere and the convective heating, which initiates deep convection along with detrained ice clouds of decreasing optical thickness. Sufficiently moist and cool upper tropospheric air parcels subjected to updraft motion initiated by gravity waves can, moreover, nucleate in-situ cirrus clouds through both homogeneous and/or heterogeneous ice nucleation (Shi et al. 2015). The median total water content (TWC) decreases with decreasing temperature from values of 10^{-3} to 10^{-2} g m^{-3} at temperatures warmer than -40°C to 10^{-5} g m^{-3} at T of -80°C (Fig. A1a), as expected by the decreasing availability of vapor for deposition growth (van Diedenhoven et al. 2020). In contrast, cloud number concentrations increase with decreasing temperatures, although the variation is not as pronounced as for TWC (Fig. A1d). The mean mass radius increases with increasing temperatures until a maximum size is reached at about -35°C. The subsequent decrease is a result of a mixture of large ice crystals with smaller and numerous cloud droplets and ice crystals formed by secondary ice production (Fig. A1g).

The model is able to reproduce most of the observed relationships as shown by the middle column. Nevertheless, the comparison reveals a general underestimation of the TWC (Fig. A1c), an underestimation of ice crystal number at temperatures colder than -60°C (Fig. A1f) and a slight underestimation of ice radius at temperatures between -60°C and -40°C (Fig. A1i). There are two possible origins of the mentioned biases:

1. the models' tendency to produce too numerous very thin ice clouds due to numerical diffusion. Such clouds, however, do not exert any significant climate forcing and therefore do not significantly bias the modeled radiative balance.

2. The biases may be partly attributed to the limitations in in-situ retrievals, given that the clouds containing low concentrations of small ice crystals cannot be detected with current particle measurement techniques (Krämer et al. 2016; Baumgardner et al. 2017).

Finally, the model lacks the Brewer-Dobson circulation, which leads to a warm bias in the tropopause region and the underestimation of the in-situ formed thin tropopause cirrus. The increase in all ice properties at the coldest modeled temperatures is a result of penetrating deep convective outflow, which is infrequent and not sampled by the observational dataset.

APPENDIX B

Relationship between brightness temperature and high cloud optical depth

In this appendix, we justify our claim from Section 3a that variability in the BT distribution reflects the evolution of anvil clouds. We examine the relationship between BT and COD using BT measurements from MODIS and cloud property, cloud top height, and COD retrievals from DARDAR-CLOUD v2.1.1. We use a full calendar year (2009) of measurements from the Tropical Western Pacific (12°S-12°N, 150°E-180°E). The MODIS 11-μm BT measurements are obtained from the Level 2 Cloud Product (Platnick et al. 2017) and have a 5×5-km resolution. The DARDAR (raDAR-liDAR) retrievals combine measurements from CloudSat's radar and CALIPSO's lidar to estimate the optical and microphysical properties of ice clouds (Delanoë and Hogan 2008). The vertical resolution is 60 m and the retrieval profiles have a horizontal spacing of about 1.1 km. We correct for the diurnal cycle of lidar sensitivity by removing cloudy pixels that were detected by the lidar only if they have a visible extinction coefficient below 0.12 km^{-1}, as described in Sokol and Hartmann (2020). For each DARDAR retrieval profile, we calculate COD for each individual cloud layer by vertically integrating the visible extinction coefficient. We then use nearest-neighbor interpolation to find the associated BT, which is only considered valid if the distance between the retrieval profile and the center of the nearest MODIS pixel is less than 3.5 km. Because the BT pixel dimensions are larger than DARDAR's horizontal resolution, each BT measurement can be associated with several COD retrievals.

There are several factors that cause the COD distribution associated with any particular BT to be wide. Some of these factors are physical. For example, the emission temperature of a cloud with fixed COD will vary depending on cloud altitude and microphysical structure, and BT can further be affected by the presence of additional cloud layers below a high, thin cirrus. Then there are the factors associated with the retrievals themselves, such as the DARDAR-CLOUD retrieval error (see Cazenave et al. (2019) for an in-depth discussion) and the fact that retrievals are only performed for ice-phase clouds. The latter's influence is likely small, since the liquid-phase clouds of the boundary layer have emission temperatures similar to that of the surface. Finally, there are factors related to the colocation methods we have used to match MODIS BT and DARDAR-CLOUD COD observations. The main source of error here is the previously noted discrepancy between the MODIS and DARDAR horizontal resolutions. Consider a hypothetical but illustrative case in which a 25-km^2 area is covered in part by a deep convective core and in part by cloud-free conditions. The core and ocean surface are associated with BTs in the realm of 200 and 300 K, respectively. The MODIS observation for this area will record a BT somewhere in between these two extremes, while some of the associated DARDAR retrievals will high COD and others will have zero COD. Despite these sources of error, we believe the analysis presented here allows for a solid understanding of the relationship between BT and COD.

The COD distributions for 10-K BT bins are shown in Fig. B1. The left column shows COD distributions for the 67% of cloudy profiles that contain one ice cloud layer. Figure B2 shows a joint histogram of BT and cloud top height (CTH) for these one-layer profiles. BTs between 190-200 K correspond to optically thick clouds with CTH above 14 km; these are deep convective cores and fresh, optically thick anvils. As BT increases from 220 to 290 K, the COD distribution shifts progressively to smaller values. At the same time, the CTH distribution varies very little, remaining centered in the 14.5-16 km range. There are a small number of observations with CTH below 10 km in the 250-290 K BT range, which we suspect are mid-level clouds with glaciated tops. But these instances are rare, suggesting that BT is controlled by high cloud optical thickness rather than cloud altitude.

The right column of Fig. B1 shows COD distributions for the 25% of cloudy profiles that contain two ice cloud layers. The uppermost cloud layers in these profiles are nearly always cirrus clouds with CTH above 10 km. As expected, their COD distributions (blue shading) follow a pattern similar to that seen in one-layer profiles. The lower layers, on the other hand, are more diverse. About half of the lower layers between 200-290 K are also cirrus clouds, with CTH above 10 km and relatively small COD. The remainder have CTH below 10 km and a wide range of COD. We speculate that these are mid-level, partially glaciated cumulus clouds that produce a COD signal corresponding only to their glaciated portions. In profiles near deep convection, it is also possible that the lower layers are mid-level outflow plumes from convective cores. Profiles with three or more layers (not shown) account for only 7% of cloudy profiles.

The warmest BT bin (290-300 K) accounts for 42% of the BT measurements in our data set. A majority of the profiles in this BT range do not contain any ice cloud layers (58%). Nearly all of the cloud-containing profiles contain one or two cirrus layers with CTH above 10 km and an average COD of 0.28.

The relationships between BT and COD examined here suggest that BT is most often a reflection of cirrus COD, with the exception of the lowest BTs associated with deep convective cores. Figure B2 supports this finding, showing that the CTH distribution in one-layer profiles is relatively constant across the observed BT range. This conclusion is to be expected, first because cirrus are the dominant cloud type in tropical convective regions, and second because cirrus altitude varies little compared to cirrus COD. Based on these findings, it is reasonable to attribute variations in the BT distribution to cirrus cloud evolution.

APPENDIX C

Anvil cloud representation binned by their respective ice water path

Free tropospheric clouds in tropical deep convective regions are dominated by anvil clouds of various COD and IWP. The evolution of tropical high clouds of significant COD typically begins with deep convective detrainment: such clouds contain the highest IWP (on the order of kg m^{-2}) and the largest COD. They quickly lose ice by precipitation and sublimation and continue their lifecycle as anvil clouds of decreasing COD until reaching the thin cirrus stage, when they become difficult to distinguish from the very thin in-situ nucleated clouds typical of the tropical tropopause layer.

We therefore group tropical high clouds by their IWP into 50 bins. Each of the bins contains the same amount of data points (2%) and thus covers exactly the same portion of the total surface area of the domain. We implemented a new model tracer that is set to 1 in all positively buoyant grid boxes with updrafts larger than 1 m s^{-1} that contain at least 10^{-3} g kg^{-1} of condensed water (either liquid or ice) and decays with a half-life of 30 minutes elsewhere. The tracer helped us estimate the time that has passed since the deep convective detrainment. The cloudy air parcels in the highest IWP bin have been detrained from deep convective updrafts about 1.7 hours earlier, on average. The cloud age increases quickly, reaching 5 hours at the 84th IWP percentile with COD of about 7 and an IWP of 100 g m^{-2} (Fig. C1a-c). Shortly thereafter, at COD of about 4 and age of 6 hours, the LW CRE becomes dominant over the SW CRE, and the cloud on average shifts from a state with net negative towards net positive CRE (Fig. C1b). The cloud continues to lose IWP until reaching values of about 10 g m^{-2} near 60th percentile bin at an average cloud age of about 7 hours. The cloud evolution slows down at this stage as indicated by the flattening of the cloud age trajectory, despite continuing to lose IWP. As a difference, the lowest 20 percentile bins result in a steep increase in cloud age, indicating a change of regime, which may be associated with optically very thin in-situ formed cirrus that may not be directly connected with the initial deep convective detrainment. Typical COD for such clouds range between 0.01 and 1, significantly lower than what shown by the COD plot in Fig. C1b, likely because of the effect of the underlying clouds. Interestingly, the SW CRE increases with increasing IWP percentile values until reaching the 95th percentile. The thickest anvils and deep convective outflow preferentially occur during the early morning hours in absence of insolation, therefore decreasing the SW CRE while still contributing to an increasing LW CRE.

References

Ansmann, A., and Coauthors, 2008: Influence of Saharan dust on cloud glaciation in southern Morocco during the Saharan Mineral Dust Experiment. *J. Geophys. Res. Atmos.*, **113 (4)**, 1–16, doi:10.1029/2007JD008785.

Bain, C. L., G. Magnusdottir, P. Smyth, and H. Stern, 2010: Diurnal cycle of the Intertropical Convergence Zone in the east Pacific. *J. Geophys. Res. Atmos.*, **115 (23)**, 1–10, doi:10.1029/2010JD014835.

Baumgardner, D., and Coauthors, 2017: Cloud Ice Properties: In Situ Measurement Challenges. *Meteorol. Monogr.*, **58**, 9.1 – 9.23, doi:10.1175/AMSMONOGRAPHS-D-16-0011.1, URL https://journals.ametsoc.org/view/journals/amsm/58/1/amsmonographs-d-16-0011.1.xml.

Berry, E., and G. G. Mace, 2014: Cloud properties and radiative effects of the Asian summer monsoon derived from A-Train data. *J. Geophys. Res. Atmos.*, **119**, 9492–9508, doi:10.1002/2014JD021458.

Bessho, K., and Coauthors, 2016: An introduction to Himawari-8/9 — Japan's new-generation geostationary meteorological satellites. *J. Meteorol. Soc. Japan*, **94 (2)**, 151–183, doi:10.2151/jmsj.2016-009.

Bowman, K. P., and M. D. Fowler, 2015: The diurnal cycle of precipitation in tropical cyclones. *J. Clim.*, **28 (13)**, 5325–5334, doi:10.1175/JCLI-D-14-00804.1.

Cazenave, Q., M. Ceccaldi, J. Delanoë, J. Pelon, S. Groß, and A. Heymsfield, 2019: Evolution of DARDAR-CLOUD ice cloud retrievals: New parameters and impacts on the retrieved microphysical properties. *Atmos. Meas. Tech.*, **12 (5)**, 2819–2835, doi:10.5194/amt-12-2819-2019.

Chen, S. S., and R. A. J. Houze, 1997: Diurnal variation and life-cycle of deep convective systems over the tropical Pacific warm pool. *Q. J. R. Meteorol. Soc.*, **123 (538)**, 357–388.

Chepfer, H., H. Brogniez, and V. Noel, 2019: Diurnal variations of cloud and relative humidity profiles across the tropics. *Sci. Rep.*, **9 (1)**, 1–9, doi:10.1038/s41598-019-52437-6, URL http://dx.doi.org/10.1038/s41598-019-52437-6.

Ciesielski, P. E., R. H. Johnson, W. H. Schubert, and J. H. Ruppert, 2018: Diurnal cycle of the ITCZ in DYNAMO. *J. Clim.*, **31 (11)**, 4543–4562, doi:10.1175/JCLI-D-17-0670.1.

Dai, A., 2001: Global precipitation and thunderstorm frequencies. Part II: Diurnal variations. *J. Clim.*, **14 (6)**, 1112–1128, doi:10.1175/1520-0442(2001)014<1112:GPATFP>2.0.CO;2.

Delanoë, J. M., and R. J. Hogan, 2008: A variational scheme for retrieving ice cloud properties from combined radar, lidar, and infrared radiometer. *J. Geophys. Res. Atmos.*, **113 (7)**, 1–21, doi:10.1029/2007JD009000.

DeMott, P. J., and Coauthors, 2010: Predicting global atmospheric ice nuclei distributions and their impacts on climate. *Proc. Natl. Acad. Sci. U. S. A.*, **107 (25)**, 11 217–11 222, doi:10.1073/pnas.0910818107.

Deng, M., and G. G. Mace, 2008: Cirrus microphysical properties and air motion statistics using cloud radar doppler moments. Part II: Climatology. *J. Appl. Meteorol. Climatol.*, **47 (12)**, 3221–3235, doi:10.1175/2008JAMC1949.1.

Dinh, T. P., D. R. Durran, and T. P. Ackerman, 2010: Maintenance of tropical tropopause layer cirrus. *J. Geophys. Res. Atmos.*, **115 (D2)**, 1–15, doi:10.1029/2009JD012735.

Dunion, J. P., C. D. Thorncroft, and C. S. Velden, 2014: The tropical cyclone diurnal cycle of mature hurricanes. *Mon. Weather Rev.*, **142 (10)**, 3900–3919, doi:10.1175/MWR-D-13-00191.1.

Durran, D. R., T. Dinh, M. Ammerman, and T. Ackerman, 2009: The Mesoscale Dynamics of Thin Tropical Tropopause Cirrus. *J. Atmos. Sci.*, **66 (9)**, 2859–2873, doi:10.1175/2009jas3046.1.

Feofilov, A. G., and C. J. Stubenrauch, 2019: Diurnal variation of high-level clouds from the synergy of AIRS and IASI space-borne infrared sounders. *Atmos. Chem. Phys.*, **19 (22)**, 13 957–13 972, doi:10.5194/acp-19-13957-2019.

Fu, R., A. D. D. Genio, and W. B. Rossow, 1990: Behavior of Deep Convective Clouds in the Tropical Pacific Deduced from ISCCP Radiances. *J.*

Clim., **3** (**10**), 1129–1152, doi:10.1175/1520-0442(1990)003<1129:BODCCI>2.0.CO;2, URL https://journals.ametsoc.org/view/journals/clim/3/10/1520-0442{_}1990{_}003{_}1129{_}bodcci{_}2{_}0{_}co{_}2.xml.

Gasparini, B., P. N. Blossey, D. L. Hartmann, G. Lin, and J. Fan, 2019: What Drives the Life Cycle of Tropical Anvil Clouds? *J. Adv. Model. Earth Syst.*, **11** (**9**), 2586–2605, doi:10.1029/2019MS001736.

Gasparini, B., and U. Lohmann, 2016: Why cirrus cloud seeding cannot substantially cool the planet. *J. Geophys. Res. Atmos.*, **121**, 4877–4893, doi:10.1002/2015JD024666.

Gasparini, B., P. J. Rasch, D. L. Hartmann, C. J. Wall, and M. Dütsch, 2021: A Lagrangian perspective on tropical anvil cloud lifecycle in present and future climate. *J. Geophys. Res. Atmos.*, **126** (**4**), 1–26, doi:10.1029/2020jd033487.

Gray, W. M., and R. W. Jacobson, 1977: Diurnal Variation of Deep Cumulus Convection. *Mon. Weather Rev.*, **105** (**9**), 1171–1188, doi:10.1175/1520-0493(1977)105<1171:DVODCC>2.0.CO;2, URL https://journals.ametsoc.org/view/journals/mwre/105/9/1520-0493{_}1977{_}105{_}1171{_}dvodcc{_}2{_}0{_}co{_}2.xml.

Hartmann, D. L., and S. E. Berry, 2017: The Balanced Radiative Effect of Tropical Anvil Clouds. *J. Geophys. Res. Atmos.*, **122**, doi:10.1002/2017JD026460.

Hartmann, D. L., B. Gasparini, S. E. Berry, and P. N. Blossey, 2018: The Life Cycle and Net Radiative Effect of Tropical Anvil Clouds. *J. Adv. Model. Earth Syst.*, **10** (**12**), 3012–3029, doi:10.1029/2018MS001484.

Heymsfield, A. J., and Coauthors, 2017: Cirrus Clouds. *Meteorol. Monogr.*, **58**, 2.1–2.26, doi: 10.1175/AMSMONOGRAPHS-D-16-0010.1, URL http://journals.ametsoc.org/doi/10.1175/AMSMONOGRAPHS-D-16-0010.1.

Hoose, C., and O. Möhler, 2012: Heterogeneous ice nucleation on atmospheric aerosols: a review of results from laboratory experiments. *Atmos. Chem. Phys.*, **12 (20)**, 9817–9854, doi: 10.5194/acp-12-9817-2012.

Houze, R. A. J., 2004: Mesoscale Convective Systems. *Rev. Geophys.*, **42 (4)**, doi: 10.1029/2004RG000150.1.INTRODUCTION, URL http://www.agu.org/pubs/crossref/2004/2004RG000150.shtml.

Iacono, M. J., J. S. Delamere, E. J. Mlawer, M. W. Shephard, S. A. Clough, and W. D. Collins, 2008: Radiative forcing by long-lived greenhouse gases: Calculations with the AER radiative transfer models. *J. Geophys. Res. Atmos.*, **113 (13)**, 2–9, doi:10.1029/2008JD009944.

Jakob, C., M. S. Singh, and L. Jungandreas, 2019: Radiative Convective Equilibrium and Organized Convection: An Observational Perspective. *J. Geophys. Res. Atmos.*, **124 (10)**, 5418–5430, doi: 10.1029/2018JD030092.

Jensen, E. J., S. C. van den Heever, and L. D. Grant, 2018: The lifecycles of ice crystals detrained from the tops of deep convection. *J. Geophys. Res. Atmos.*, **123 (17)**, 9624– 9634, doi:10.1029/2018JD028832, URL http://doi.wiley.com/10.1029/2018JD028832.

Jensen, E. J., and Coauthors, 2017: The NASA Airborne Tropical TRopopause EXperiment (ATTREX): High-Altitude Aircraft Measurements in the Tropical Western Pacific. *Bull. Am. Meteorol. Soc.*, **98 (1)**, 129–143, doi:10.1175/BAMS-D-14-00263.1, URL http://journals.ametsoc.org/doi/abs/10.1175/BAMS-D-14-00263.1.

Kärcher, B., J. Hendricks, and U. Lohmann, 2006: Physically based parameterization of cirrus cloud formation for use in global atmospheric models. *J. Geophys. Res.*, **111 (D1)**, D01 205, doi:10.1029/2005JD006219.

Khairoutdinov, M. F., and D. A. Randall, 2003: Cloud Resolving Modeling of the ARM Summer 1997 IOP : Model Formulation , Results , Uncertainties , and Sensitivities. *J. Atmos. Sci.*, **60**, 607–625, doi:10.1175/1520-0469(2003)060<0607:CRMOTA>2.0.CO;2, URL http://journals.ametsoc.org/doi/pdf/10.1175/1520-0469(2003)060{\%}3C0607:CRMOTA{\%}3E2.0.CO;2.

Krämer, M., and Coauthors, 2016: A microphysics guide to cirrus clouds – Part 1: Cirrus types. *Atmos. Chem. Phys.*, **16 (21)**, 3463–3483, doi:10.5194/acpd-15-31537-2015, URL http://www.atmos-chem-phys-discuss.net/15/31537/2015/.

Krämer, M., and Coauthors, 2020: A Microphysics Guide to Cirrus – Part II: Climatologies of Clouds and Humidity from Observations. *Atmos. Chem. Phys.*, **20 (21)**, 12 569–12 608, doi:10.5194/acp-20-12569-2020.

Kraus, E. B., 1963: The Diurnal Precipitation Change over the Sea. *J. Atmos. Sci.*, **20 (6)**, 551–556, doi:10.1175/1520-0469(1963)020<0551:TDPCOT>2.0.CO;2, URL https://journals.ametsoc.org/view/journals/atsc/20/6/1520-0469{_}1963{_}020{_}0551{_}tdpcot{_}2{_}0{_}co{_}2.xml.

Liu, X., and J. E. Penner, 2005: Ice nucleation parameterization for global models. *Meteorol. Zeitschrift*, **14 (4)**, 499–514, doi:10.1127/0941-2948/2005/0059, URL http://openurl.ingenta.com/content/xref?genre=article{\&}issn=0941-2948{\&}volume=14{\&}issue=4{\&}spage=499.

Lohmann, U., F. Lüond, and F. Mahrt, 2016: *An introduction to clouds: From the microscale to climate*. Cambridge University Press, 505 pp.

Mace, G. G., M. Deng, B. Soden, and E. Zipser, 2006: Association of Tropical Cirrus in the 10–15-km Layer with Deep Convective Sources: An Observational Study Combining Millimeter Radar Data and Satellite-Derived Trajectories. *J. Atmos. Sci.*, **63 (2)**, 480–503, doi:10.1175/JAS3627.1.

Mapes, B. E., T. T. Warner, and M. Xu, 2003: Diurnal patterns of rainfall in northwestern South America. Part II: Model simulations. *Mon. Weather Rev.*, **131 (5)**, 813–829, doi:10.1175/1520-0493(2003)131<0813:DPORIN>2.0.CO;2.

Meyers, M. P., P. J. Demott, and W. R. Cotton, 1992: New primary ice-nucleation parameterizations in an explicit cloud model. *J. Appl. Meteorol.*, **31 (7)**, 708–721, doi:10.1175/1520-0450(1992)031<0708:NPINPI>2.0.CO;2.

Mlawer, E. J., J. Taubman, P. D. Brown, M. J. Iacono, and S. A. Clough, 1997: Radiative transfer for inhomogeneous atmospheres: RRTM, a validated correlated-k model for the longwave. *J. Geophys. Res.*, **102 (D14)**, 16 663–16 682, doi:doi:10.1029/97JD00237.

Morrison, H., and J. A. Milbrandt, 2015: Parameterization of Cloud Microphysics Based on the Prediction of Bulk Ice Particle Properties. Part I: Scheme Description and Idealized Tests. *J. Atmos. Sci.*, **72 (1)**, 287–311, doi:10.1175/JAS-D-14-0065.1, URL http://journals.ametsoc.org/doi/10.1175/JAS-D-14-0065.1.

Murphy, D. M., and T. Koop, 2005: Review of the vapour pressures of ice and supercooled water for atmospheric applications. *Q. J. R. Meteorol. Soc.*, **131 (608)**, 1539–1565, doi:10.1256/qj.04.94, URL http://doi.wiley.com/10.1256/qj.04.94.

Nesbitt, S. W., and E. J. Zipser, 2003: The Diurnal Cycle of Rainfall and Convective Intensity according to Three Years of TRMM Measurements. *J. Clim.*, **16 (10)**, 1456–1475, doi:10.1175/1520-0442-16.10.1456.

Pan, L. L., and Coauthors, 2017: The convective transport of active species in the tropics (Contrast) experiment. *Bull. Am. Meteorol. Soc.*, **98 (1)**, 106–128, doi:10.1175/BAMS-D-14-00272.1.

Platnick, S., and Coauthors, 2017: The MODIS Cloud Optical and Microphysical Products: Collection 6 Updates and Examples From Terra and Aqua. *IEEE Trans. Geosci. Remote Sens.*, **55 (1)**, 502–525, doi:10.1109/TGRS.2016.2610522.

Protopapadaki, S. E., C. J. Stubenrauch, and A. G. Feofilov, 2017: Upper Tropospheric Cloud Systems Derived from IR Sounders: Properties of Cirrus Anvils in the Tropics. *Atmos. Chem. Phys.*, **17**, 3845–3859, doi:10.5194/acp-17-3845-2017, URL www.atmos-chem-phys.net/17/3845/2017/.

Randall, D. A., Harshvardhan, and D. A. Dazlich, 1989: Diurnal Variability of the Hydrologic Cycle in a General Circulation Model. *J. Atmos. Sci.*, **48 (1)**, 40–62, doi:10.1175/1520-0469(1991)048<0040:DVOTHC>2.0.CO;2, URL https://journals.ametsoc.org/view/journals/atsc/48/1/1520-0469{_}1991{_}048{_}0040{_}dvothc{_}2{_}0{_}co{_}2.xml.

Ruppert, J. H., and C. Hohenegger, 2018: Diurnal circulation adjustment and organized deep convection. *J. Clim.*, **31 (12)**, 4899–4916, doi:10.1175/JCLI-D-17-0693.1.

Ruppert, J. H., and D. Klocke, 2019: The two diurnal modes of tropical upward motion. *Geophys. Res. Lett.*, **46**, 2911–2921, doi:10.1029/2018GL081806, URL http://doi.wiley.com/10.1029/2018GL081806.

Ruppert, J. H., and M. E. O'Neill, 2019: Diurnal Cloud and Circulation Changes in Simulated Tropical Cyclones. *Geophys. Res. Lett.*, **46 (1)**, 502–511, doi:10.1029/2018GL081302.

Ruppert, J. H., A. A. Wing, X. Tang, and E. L. Duran, 2020: The critical role of cloud–infrared radiation feedback in tropical cyclone development. *Proc. Natl. Acad. Sci. U. S. A.*, **117 (45)**, 27 884–27 892, doi:10.1073/pnas.2013584117.

Schmidt, C. T., and T. J. Garrett, 2013: A Simple Framework for the Dynamic Response of Cirrus Clouds to Local Diabatic Radiative Heating. *J. Atmos. Sci.*, **70 (5)**, 1409–1422, doi:10.1175/JAS-D-12-056.1, URL http://journals.ametsoc.org/doi/abs/10.1175/JAS-D-12-056.1.

Shi, X., X. Liu, and K. Zhang, 2015: Effects of preexisting ice crystals on cirrus clouds and comparison between different ice nucleation parameterizations with the Community Atmosphere Model (CAM5). *Atmos. Chem. Phys.*, **15 (3)**, 1503–1520, doi:10.5194/acp-15-1503-2015, URL http://www.atmos-chem-phys-discuss.net/14/17635/2014/.

Sokol, A. B., and D. L. Hartmann, 2020: Tropical Anvil Clouds: Radiative Driving Toward a Preferred State. *J. Geophys. Res. Atmos.*, **125 (21)**, e2020JD033 107, doi:https://doi.org/10.1029/2020JD033107, URL https://agupubs.onlinelibrary.wiley.com/doi/abs/10.1029/2020JD033107.

Tao, W.-K., S. Lang, J. Simpson, C.-H. Sui, B. Ferrier, and M.-D. Chou, 1996: Mechanisms of Cloud-Radiation Interaction in the Tropics and Midlatitudes. *J. Atmos. Sci.*, **53 (18)**, 2624–2651, doi:10.1175/1520-0469(1996)053<2624:MOCRII>2.0.CO;2, URL https://journals.ametsoc.org/view/journals/atsc/53/18/1520-0469{_}1996{_}053{_}2624{_}mocrii{_}2{_}0{_}co{_}2.xml.

van Diedenhoven, B., A. S. Ackerman, A. M. Fridlind, B. Cairns, and J. Riedi, 2020: Global Statistics of Ice Microphysical and Optical Properties at Tops of Optically Thick Ice Clouds. *J.*

Geophys. Res. Atmos., **125 (6)**, 1–21, doi:10.1029/2019JD031811.

Wall, C. J., J. R. Norris, B. Gasparini, W. L. Smith Jr., M. M. Thieman, and O. Sourdeval, 2020: Observational Evidence that Radiative Heating Modifies the Life Cycle of Tropical Anvil Clouds. *J. Clim.*, **33**, 8621–8640, doi:https://doi.org/10.1175/JCLI-D-20-0204.1, URL https://doi.org/10.1175/JCLI-D-20-0204.1.

Zipser, E. J., and M. A. LeMone, 1980: Cumulonimbus Vertical Velocity Events in GATE. Part II: Synthesis and Model Core Structure. *J. Atmos. Sci.*, **37 (11)**, 2458–2469, doi:10.1175/1520-0469(1980)037<2458:CVVEIG>2.0.CO;2, URL https://journals.ametsoc.org/view/journals/atsc/37/11/1520-0469{_}1980{_}037{_}2458{_}cvveig{_}2{_}0{_}co{_}2.xml.

LIST OF TABLES

Table 1. List of abbreviations.

Abbreviation	**Meaning**
ACRE	atmospheric cloud radiative effect
BT	brightness temperature
CRE	cloud radiative effect
CNC	cloud number concentration
COD	cloud optical depth
CTH	cloud top height
LT	local time
IWC	ice water content
IWP	ice water path
LW	longwave radiation
RCE	radiative-convective equilibrium
R_{cloud}	cloud mean mass radius
RH_{ice}	relative humidity with respect to ice
SAM	System for Atmospheric Modeling
SW	shortwave radiation
TWC	total water content

TABLE 2. A list of performed simulations.

Simulation	insolation	Description
1. Cloud in the middle of the domain		
ctrl-real	realistic diurnal cycle	full physics, 24 simulations initialized between 0 and 23 LT
small-real	realistic diurnal cycle	full physics, as ctrl-real but with inital cloud diameter of 30 km
large-real	realistic diurnal cycle	full physics, as ctrl-real but with inital cloud diameter of 120 km
day/night-only	day (1300 W m^{-2}) and night (0 W m^{-2})	full physics, as ctrl-real but with constant insolation
no-freezing	day (1300 W m^{-2}) and night (0 W m^{-2})	as day/night-only but with no ice nucleation
no-ACRE	day (1300 W m^{-2}) and night (0 W m^{-2})	as day/night-only but with no ACRE
no-sublimation	day (1300 W m^{-2}) and night (0 W m^{-2})	as day/night-only but with no sublimation
no-sedimentation	day (1300 W m^{-2}) and night (0 W m^{-2})	as day/night-only but with no sedimentation
2. RCE	realistic diurnal cycle	50-day simulation in radiative-convective equilibrium

LIST OF FIGURES

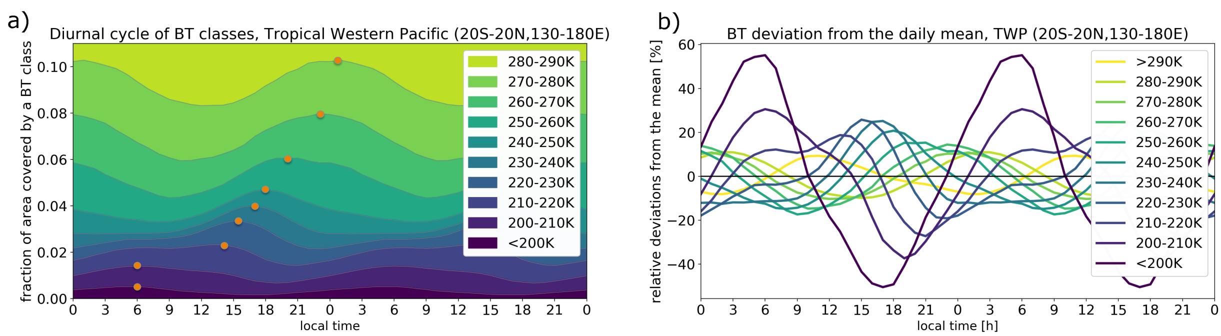

995 FIG. 1. Diurnal cycle of 10 K brightness temperature (BT) bins in the Tropical Western Pacific; (a) variations
996 of occurrence frequency and (b) relative deviations from the diurnal means. The diurnal peak in occurrence
997 frequency in of each BT bin in (a) is marked by orange dots.

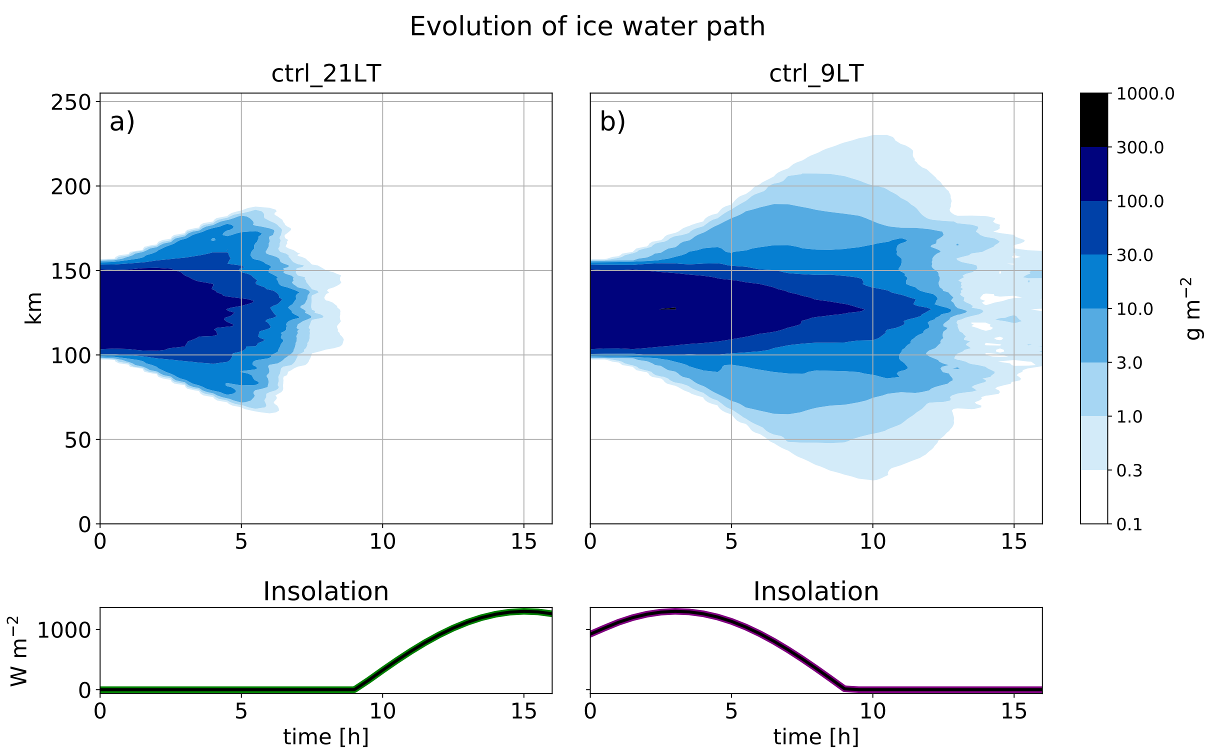

FIG. 2. Time evolution of ice water path for a cloud initialized at 21 LT (a) and 9 LT (b), averaged over one of the two horizontal dimensions. The respective insolation profiles are shown in the lower panels.

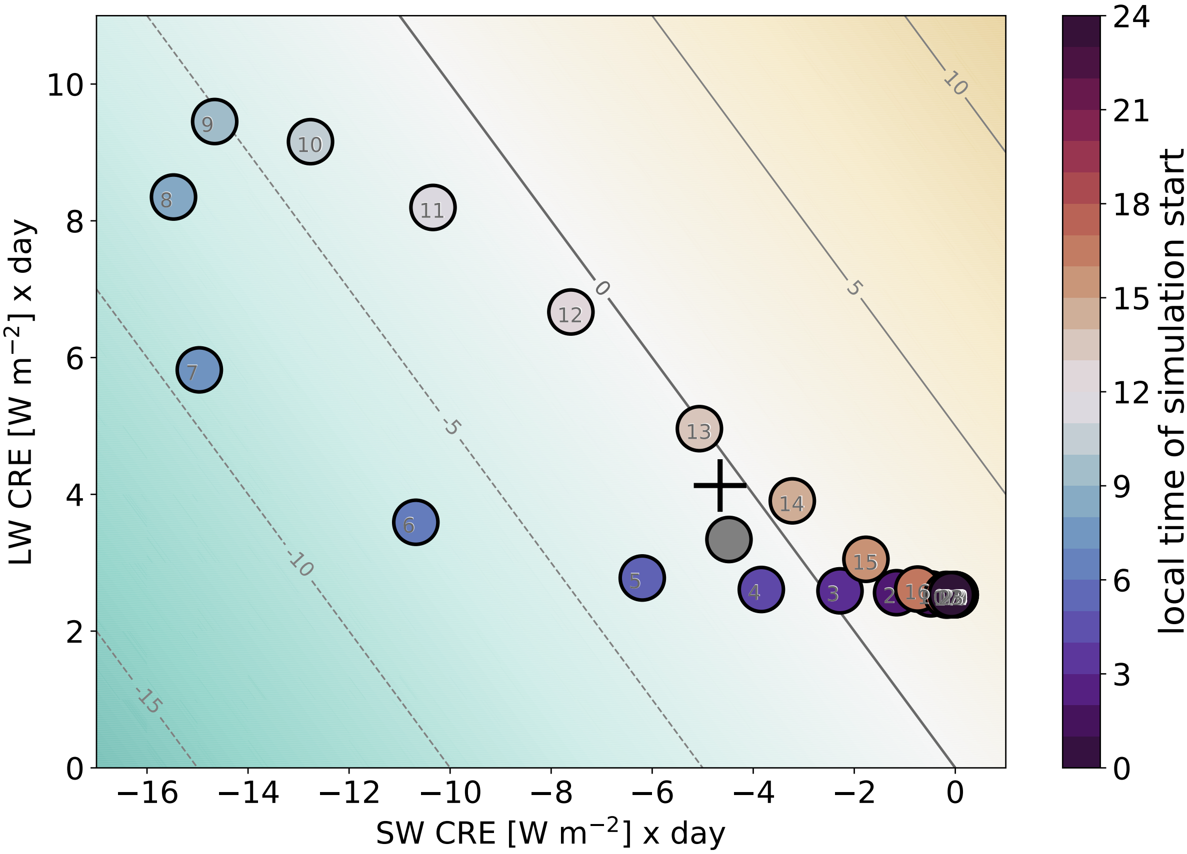

FIG. 3. Domain- and time-integrated cloud radiative effect (CRE) for simulations with variable local time of simulation start. The background color represents the net integrated CRE. The gray circle represents the values for the simulation at perpetual diurnally averaged insolation. The black plus sign represents the average of all 24 simulations.

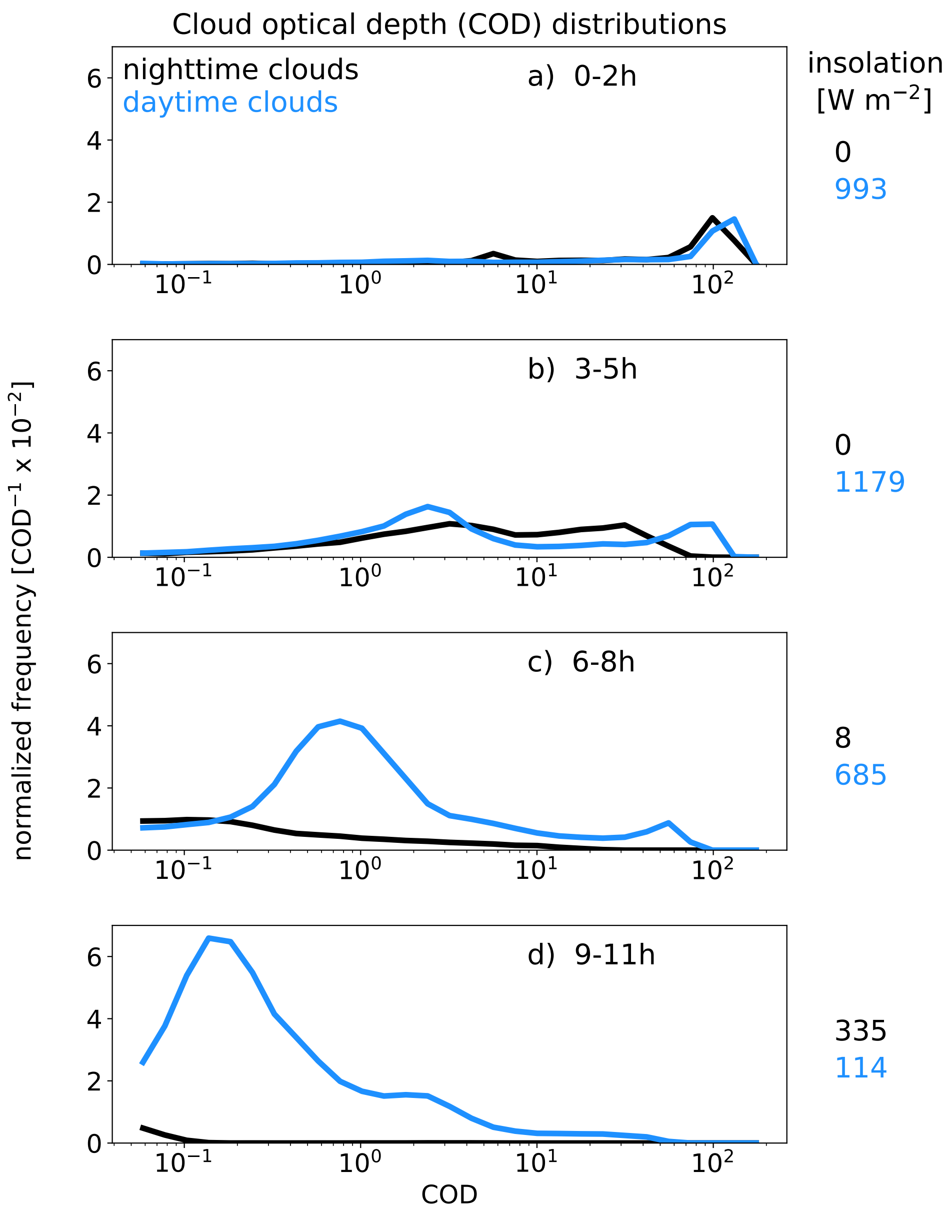

FIG. 4. Evolution of the cloud optical depth distribution over the anvil lifecycle. Daytime anvil composite represents simulations started between 7 and 11 LT, nighttime composite represents simulations started between 19 and 23 LT. (a)–(d) The fraction of the domain covered by each COD bin for different values of cloud age. A cloud age of zero corresponds to the starting time for each of the simulations.

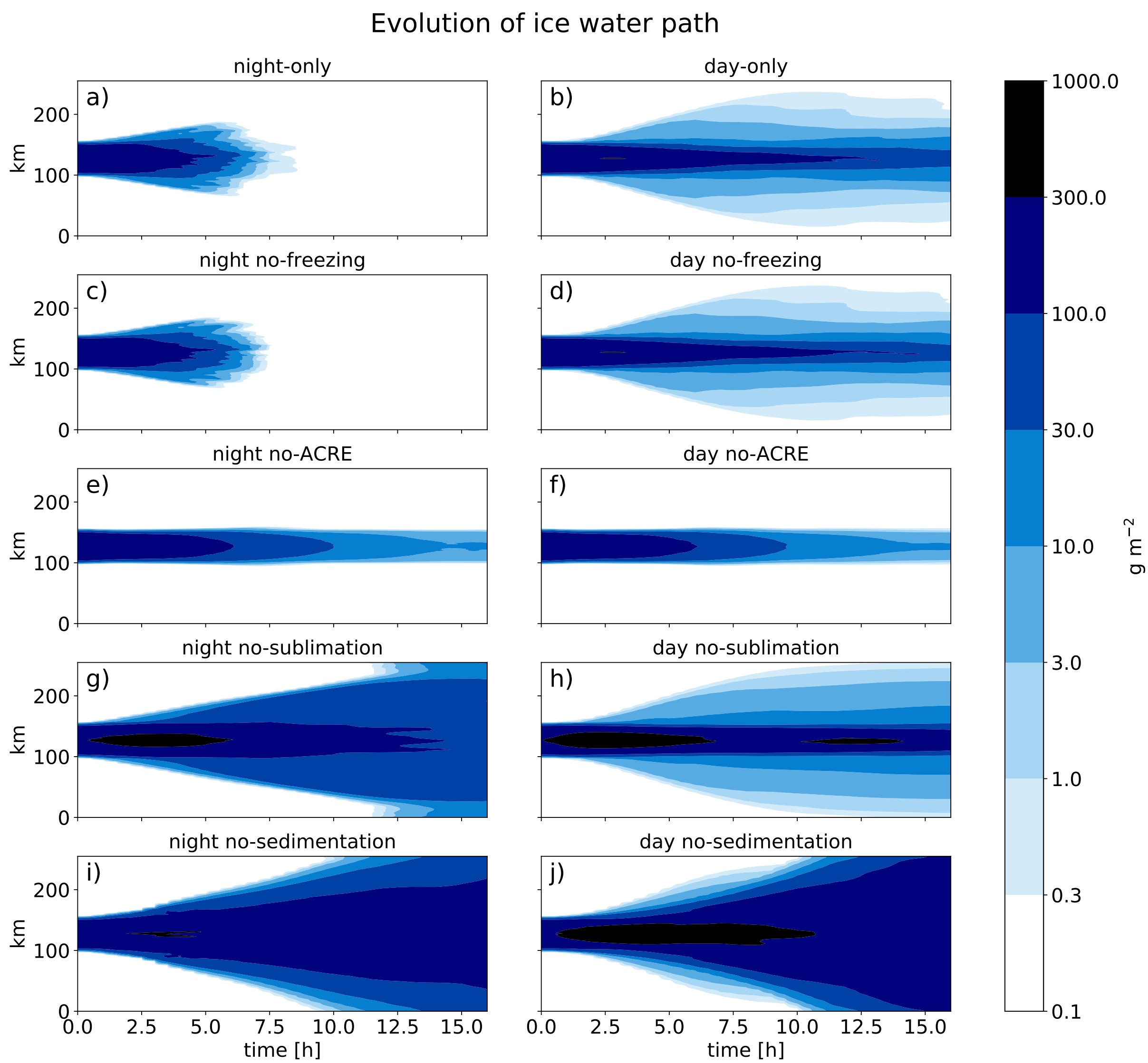

FIG. 5. Time evolution of ice water path averaged over one of the two horizontal dimensions for the control simulations (a,b) and 4 sensitivity experiments (c-j) in perpetual night (no insolation) and perpetual midday conditions (insolation of 1300 W m^{-2}).

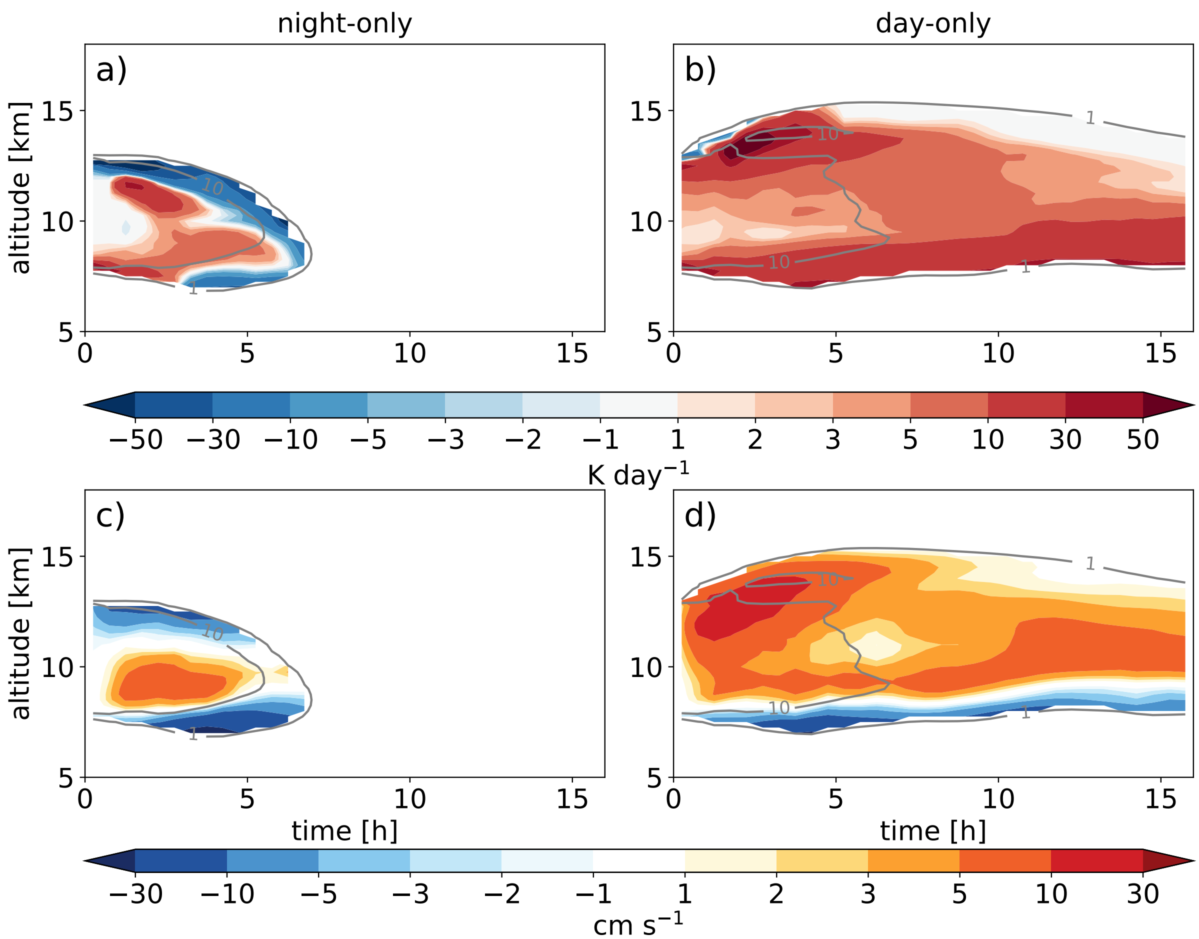

FIG. 6. Time evolution of radiative heating (a,b) and vertical velocity (c,d) for clouds in perpetual night (a,c) and perpetual midday conditions (insolation of 1300 W m^{-2}) averaged over the cloudy portion of the domain (where condensed water >10 mg kg^{-1}). Gray contour lines represent ice mixing ratio isolines of 1 and 10 mg kg^{-1}.

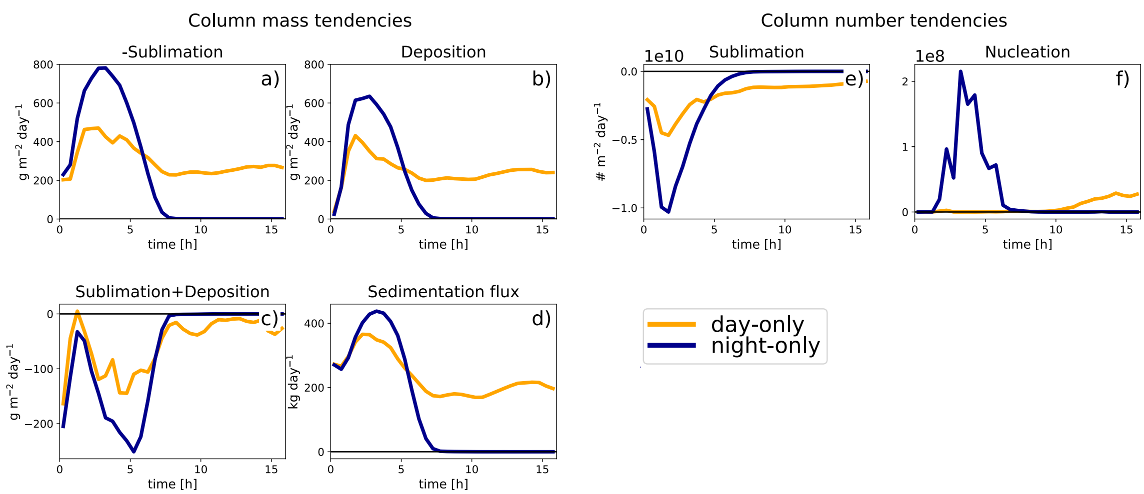

FIG. 7. Selected column vertically integrated mass (a-c) and number (e-g) microphysical tendencies, including the sedimentation flux (d) for perpetual day and night simulations.

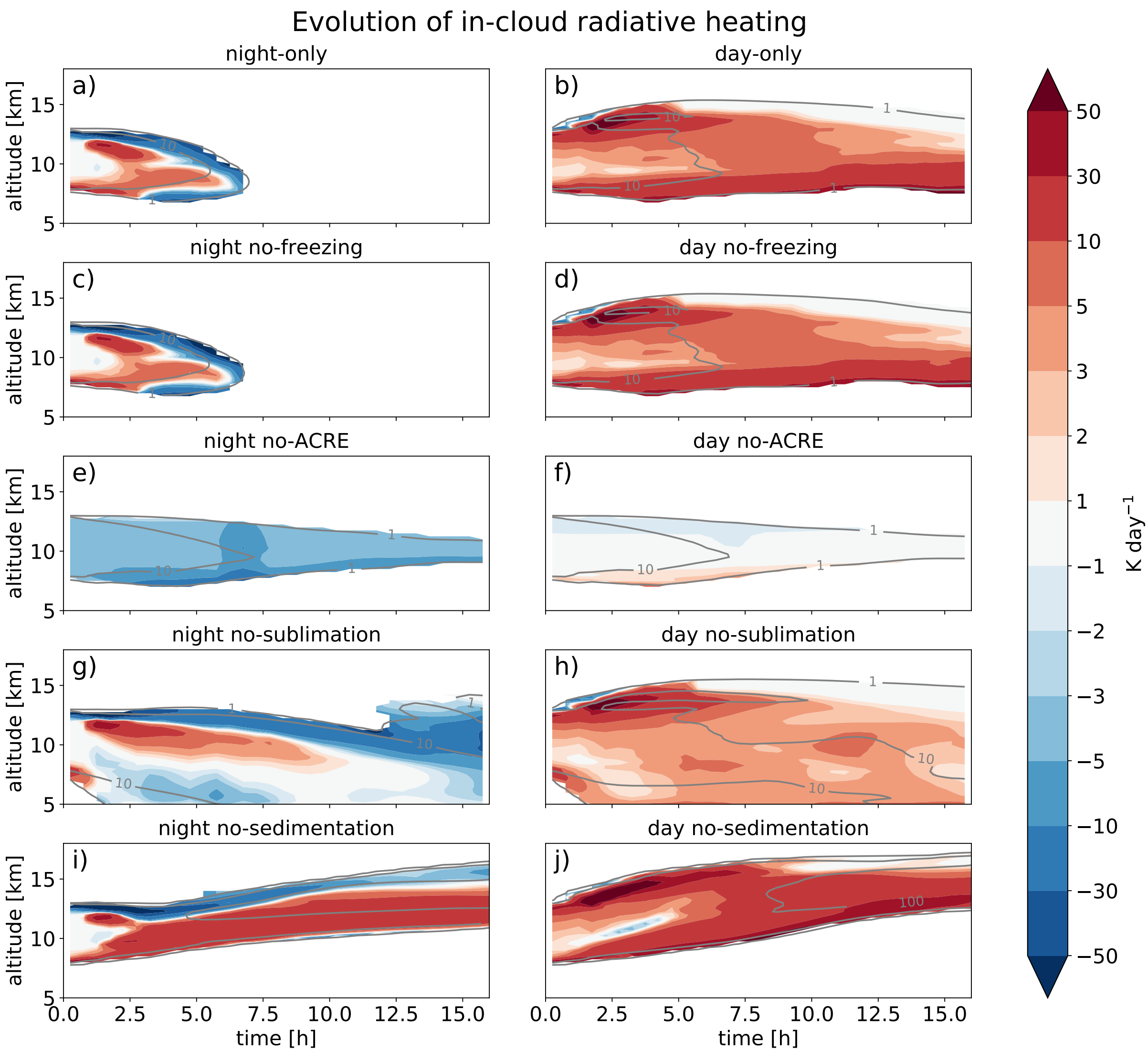

Fig. 8. Time evolution of in-cloud radiative heating for perpetual day and night control (a-b) and 4 sensitivity experiments (c-j). Gray contour lines represent ice mixing ratio contours of 1 and 10 mg kg^{-1}.

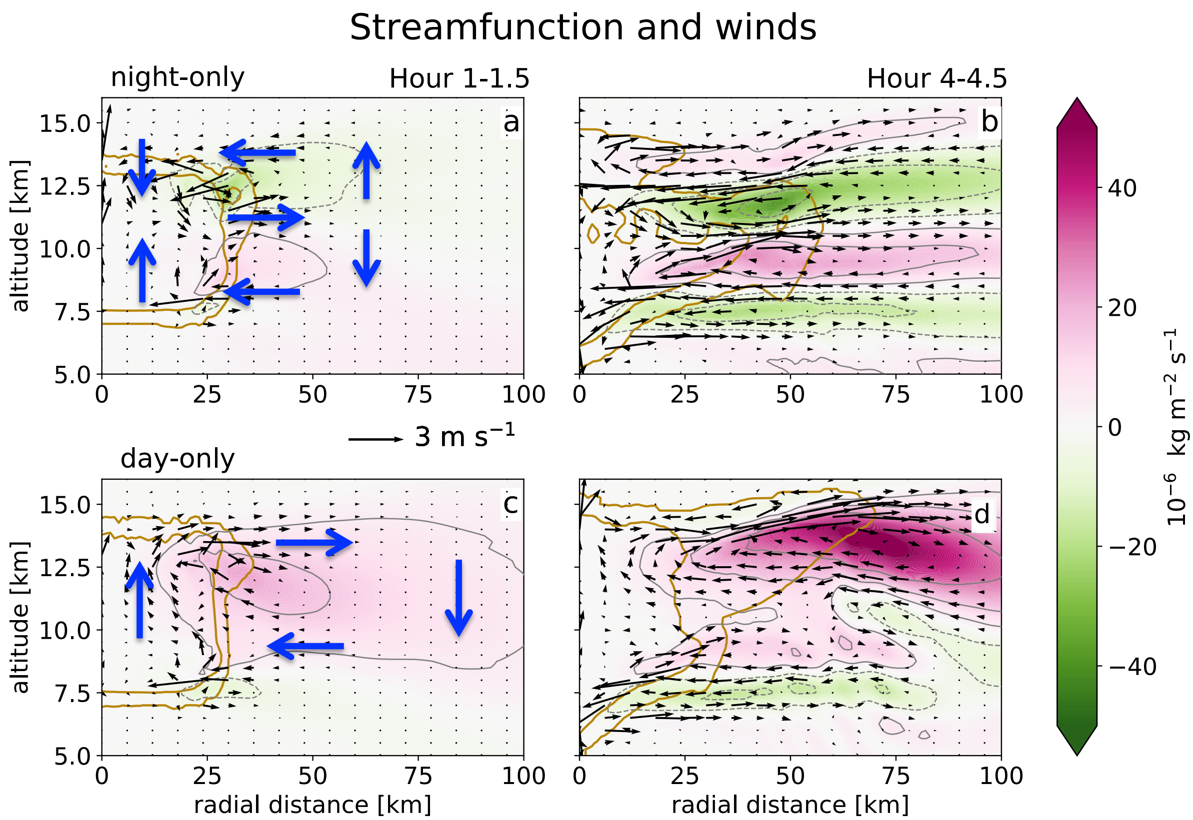

1019 FIG. 9. Wind vectors and streamfunction (in filled contours) for perpetual night (a,b) and day (c,d) simulations

1020 at hour 1-1.5 and 4-4.5 of the evolution. The key circulations are on panels a) and c) highlighted by blue arrows.

1021 Brown contour lines represent ice mixing ratio contours of 100 and 0.1 mg kg^{-1}.

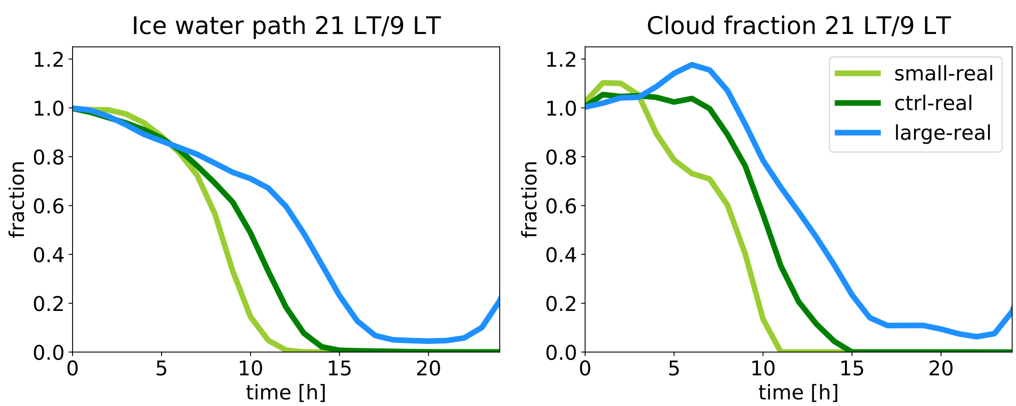

1022 FIG. 10. The ratio of IWP (a) and cloud fraction (b) between simulations started at 21 LT and 9 LT. A fraction
1023 smaller than 1 means that the selected quantity is at the given time smaller in the simulation started at 21 LT
1024 compared to the simulation started at 9 LT. A fraction larger than 1 means that the selected quantity is at the
1025 given time larger in the simulation started at 21 LT compared to the simulation started at 9 LT. The small-real
1026 initial cloud diameter is 30 km, ctrl-real is 60 km, and large-real is 120 km.

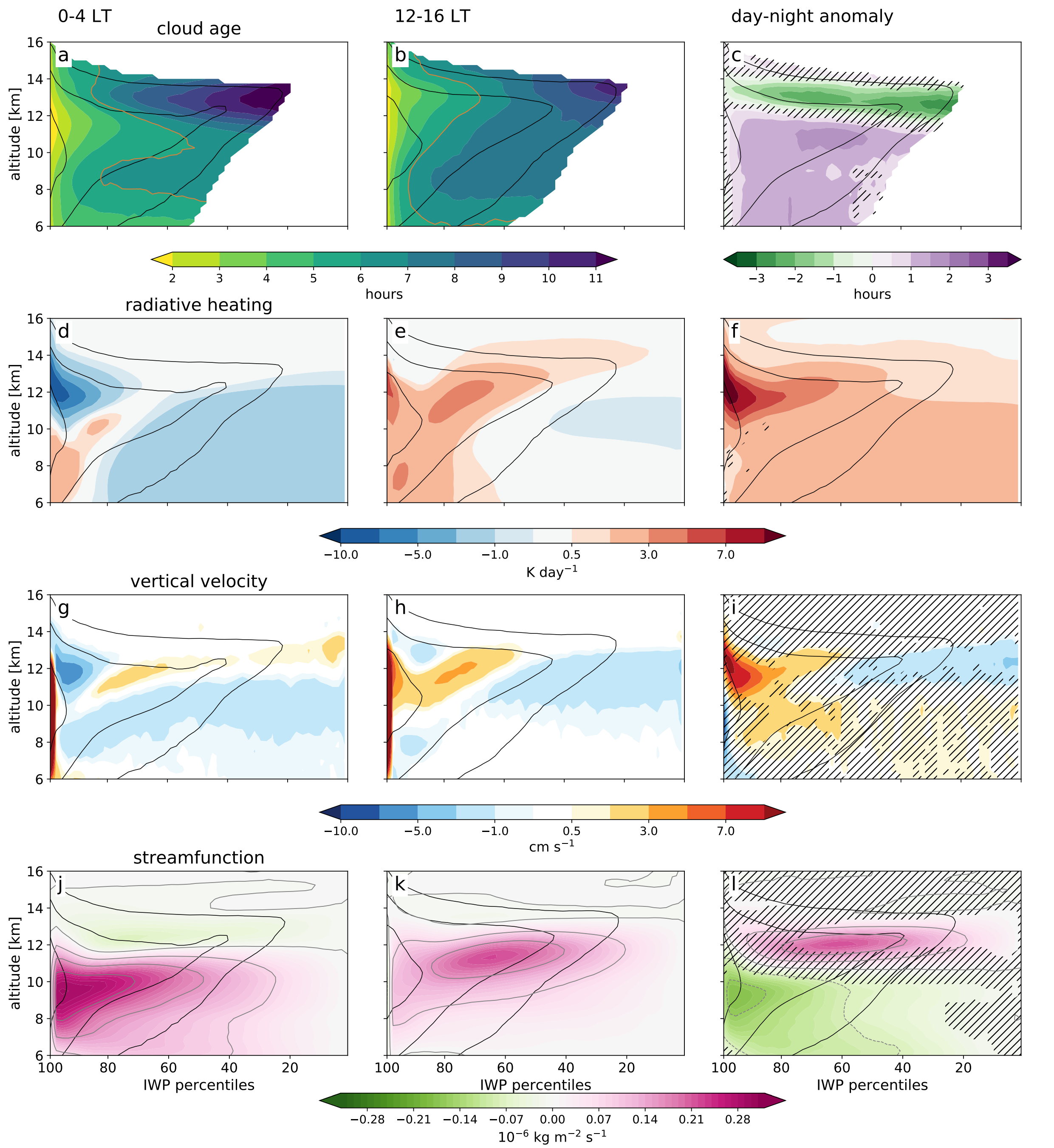

FIG. 11. Cloud age (a-c), radiative heating (d-f), vertical velocity (h-i) and streamfunction (j-l) binned by ice water path (IWP) for night (0-4 local time, left column) and day (12-16 local time, middle column). The right column represents the absolute anomaly between day (left column) and night (middle column) quantities. The black contour lines represent cloud fraction of 0.9, 0.5, and 0.1. Hatching is applied in the right column to areas that not significant at 1 percent level.

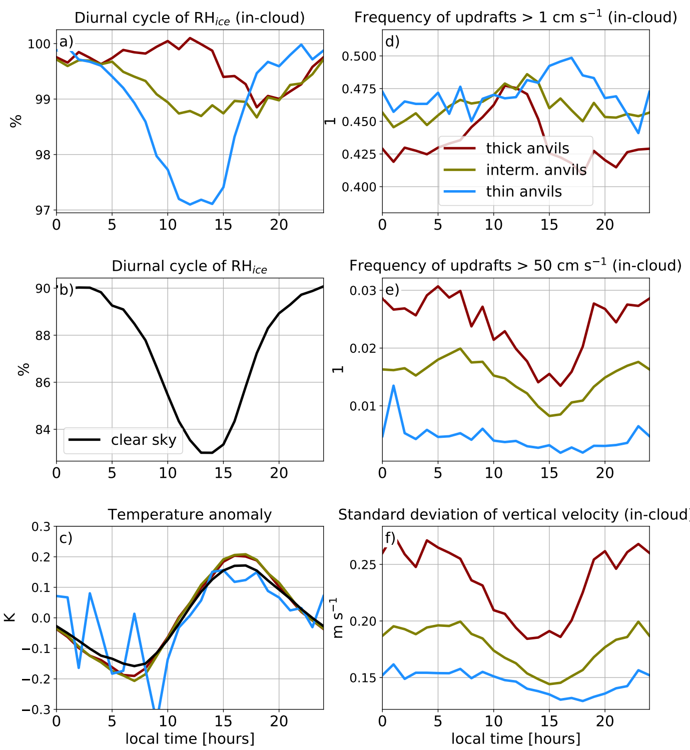

FIG. 12. Diurnal cycle of RH$_{ice}$ for thick, intermediate and thin anvil clouds (a) and clear sky regions (b) averaged for altitudes between 10 and 15 km. The deviation of the temperature from the mean over the diurnal cycle between 10-15 km altitude is plotted in panel (c). Panels d-f show an in-cloud vertical velocity analysis for the upper portions of the anvil clouds (12-15 km altitude), namely: the frequency of vertical velocity > 1 cm s^{-1} (d), frequency of vertical velocity > 50 cm s^{-1} (e), standard deviation of vertical velocity (f).

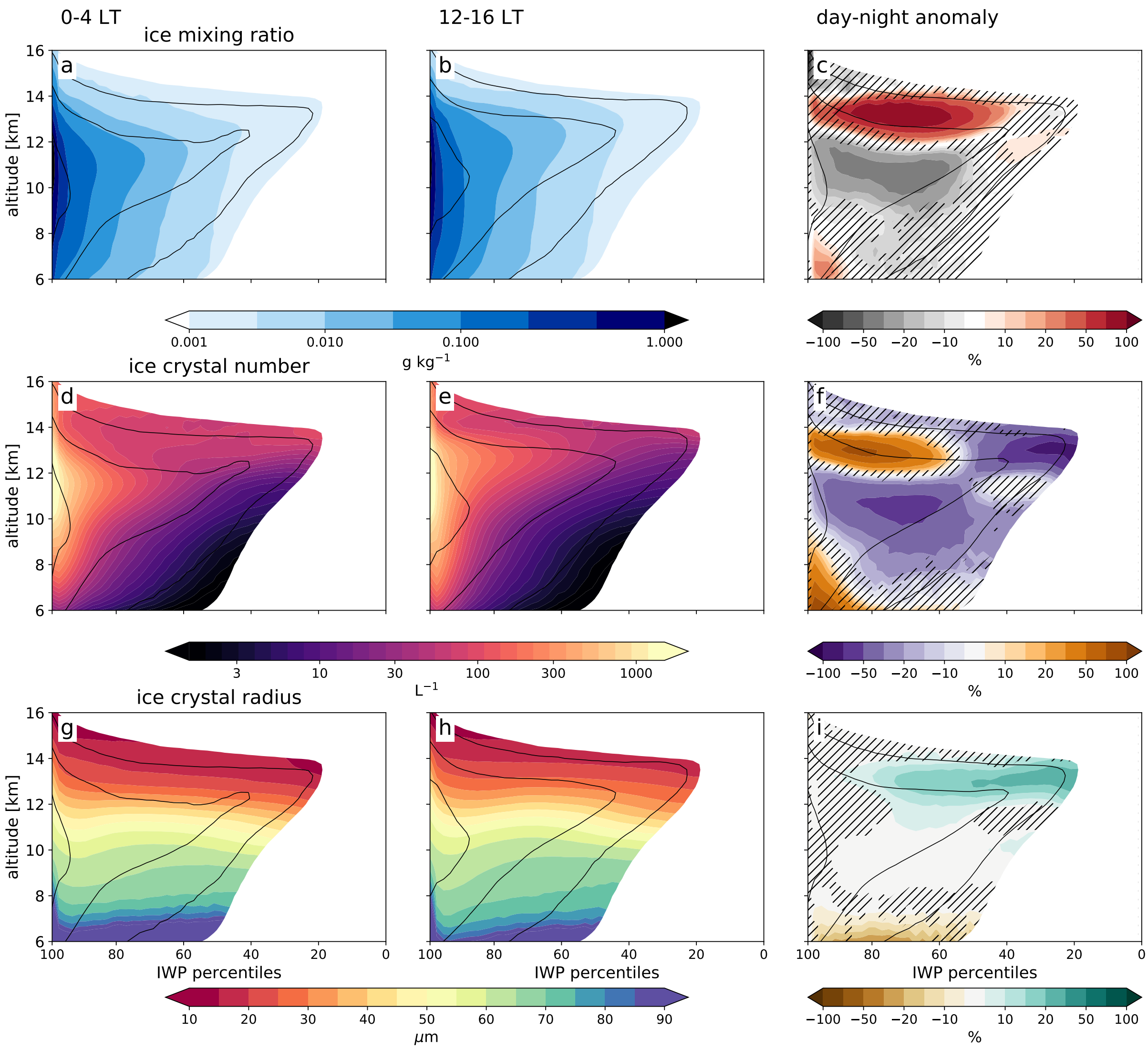

Fɪɢ. 13. In-cloud ice mixing ratio (a-c), ice crystal number (d-f), and ice crystal radius (g-i) binned by ice water path (IWP) for night (0-4 local time, left column) and day (12-16 local time, middle column). The values are averaged over the cloudy portion of the domain (condensed water >1 mg kg^{-1}). The right column represents the absolute anomaly between day (left column) and night (middle column) quantities. The black contour lines represent cloud fraction of 0.9, 0.5, and 0.1. Hatching is applied in the right column to areas that not significant at 1 percent level.

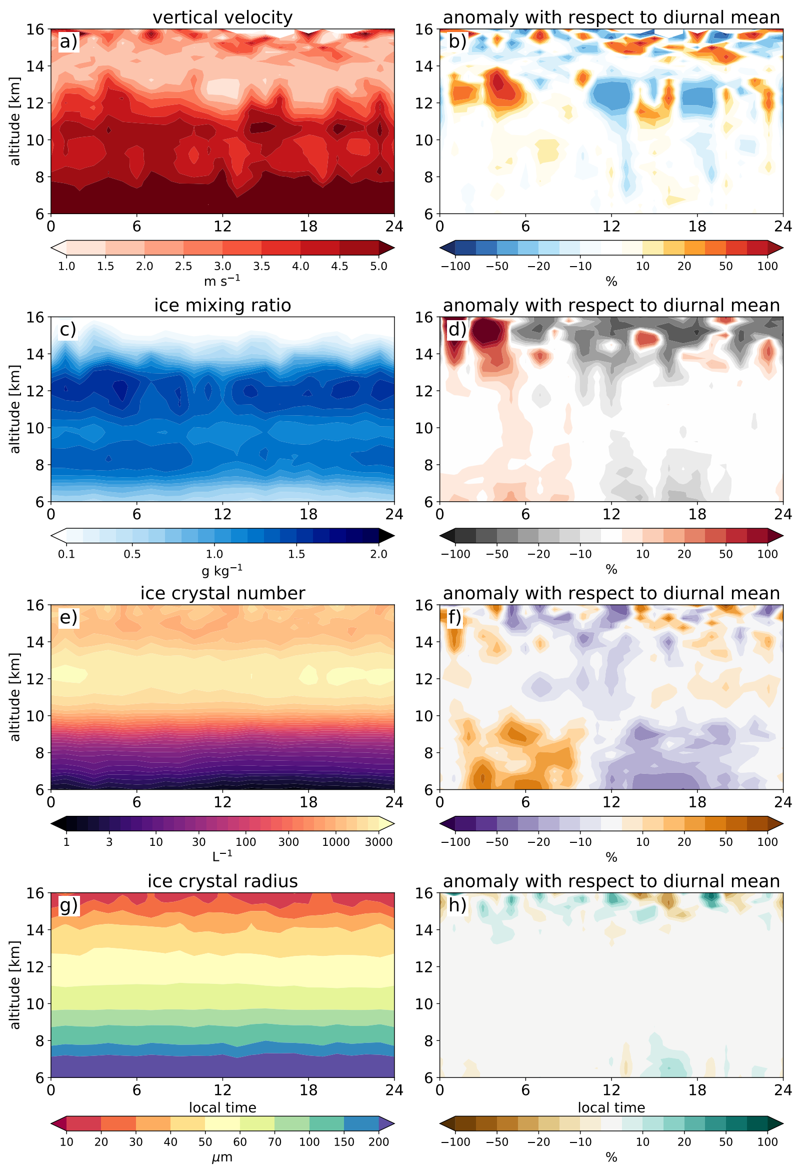

FIG. 14. Diurnal variations of the mean deep convective updraft velocity, diagnosed only for updrafts stronger than 1 m s^{-1} and of the microphysical properties for clouds within the first hour after detrainment. The right column represents the anomalies from the diurnal average values computed separately for each vertical layer.

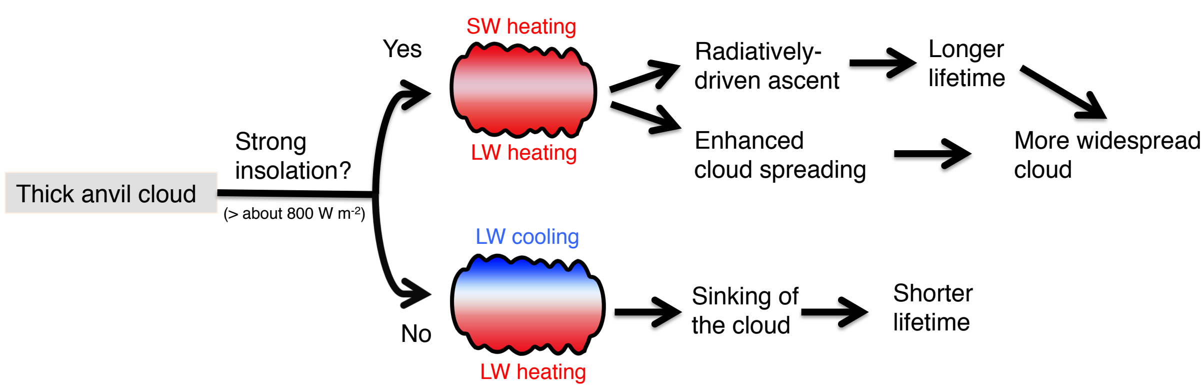

FIG. 15. Main mechanisms that lead to diurnal changes in anvil clouds.

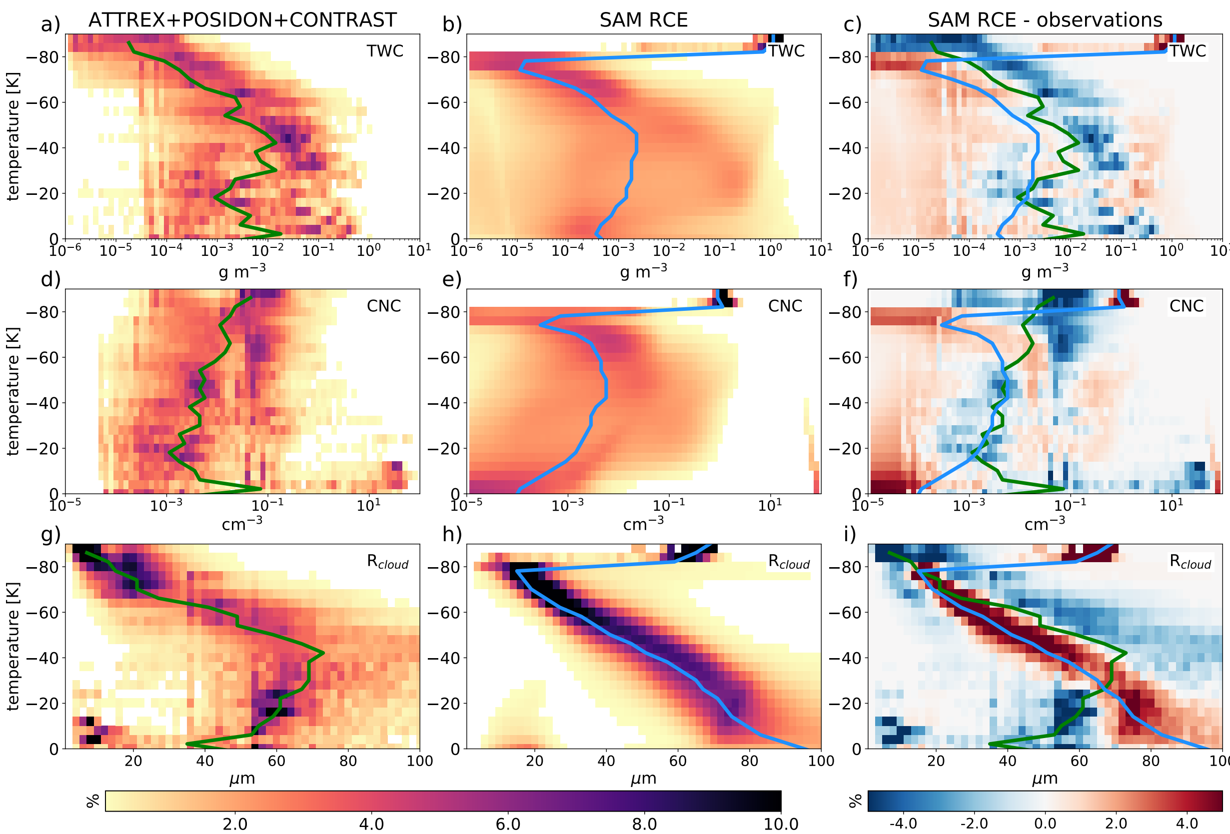

Fig. A1. Total water content (TWC, a-c), cloud number concentration (CNC, d-f), and cloud mean mass radius (R_{cloud}, g-i) from in-situ measurements sampled in 3 tropical Pacific field campaigns (left column) and from the RCE model simulation (middle column). The mass mean radius is defined as $R_{cloud} = (3TWC/4\pi\rho N_{cloud})^{1/3}$. The data are sorted in 4°C temperature bins. The colors represent the occurrence frequency of one of the 3 cloud properties, normalized to reach 100% in each of the temperature bins. The green and blue lines represent the median values of the in-situ and model data in all subplots, including the right column. The colors in the right column represent the occurrence frequency anomaly between the first two columns.

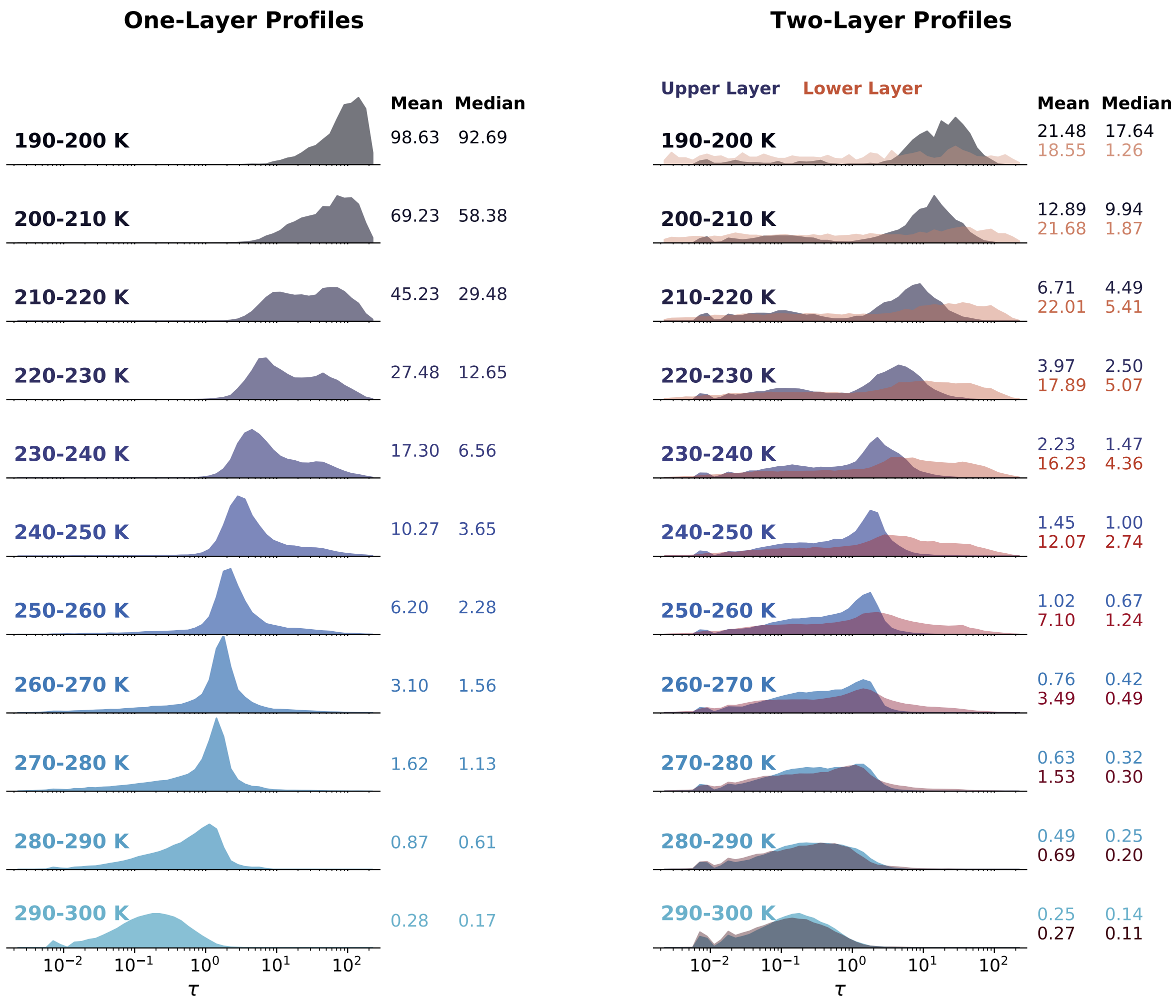

Fig. B1. Distributions of cloud optical depth for different brightness temperature classes. Left column: retrieval profiles with one ice cloud layer. Right column: profiles wth two ice cloud layers.

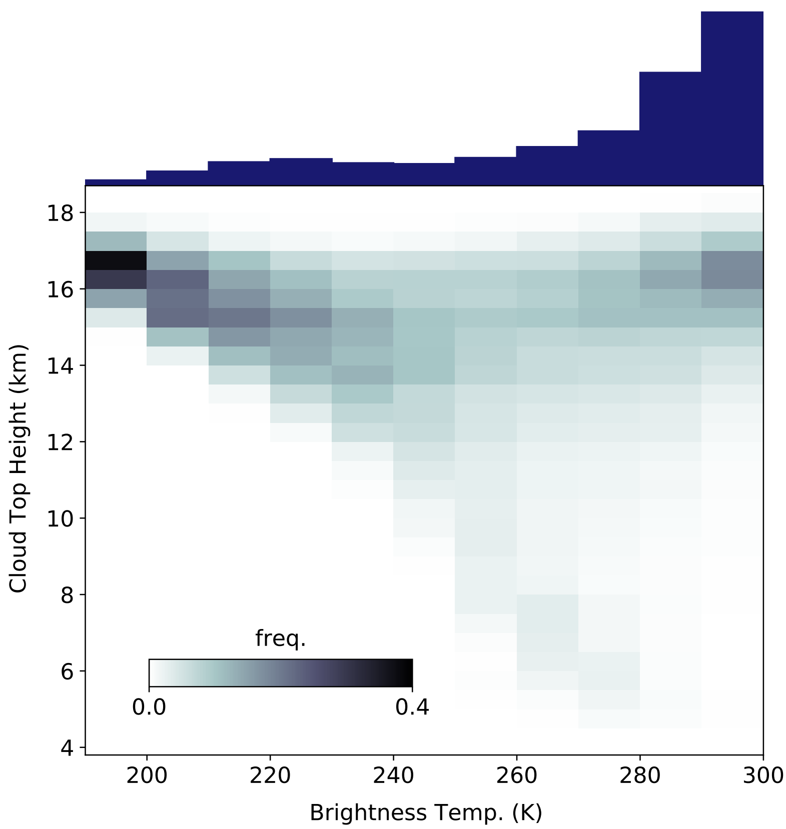

1055 Fig. B2. Joint histogram of brightness temperature and cloud top for profiles with a single ice cloud layer. The
1056 histogram is normalized by brightness temperature bin such that the values in each column sum to unity. The
1057 navy bar chart shows the relative frequency of each BT bin in the study region. Data are for both day and night.

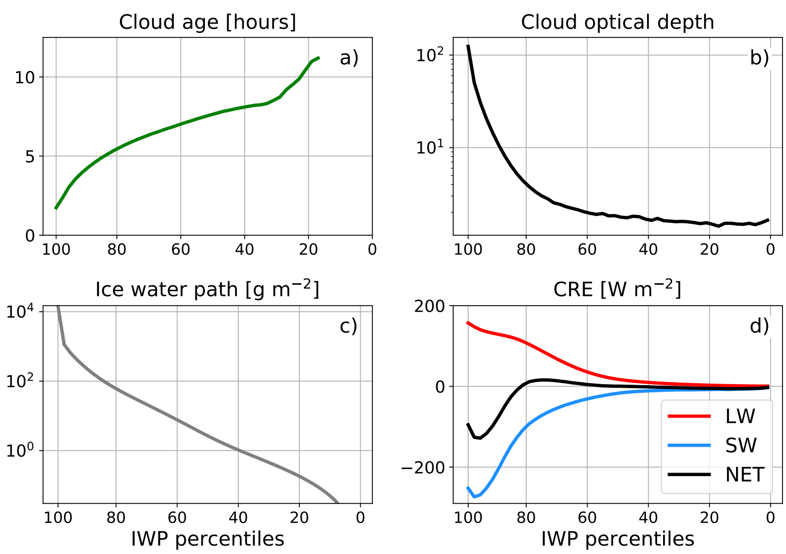

Fig. C1. Anvil cloud age (a), cloud optical depth (b), ice water path (IWP) (c) and top of the atmosphere cloud radiative effects (CRE) (d) binned by ice water path percentiles.